A Quasi-Equilibrium Tropical Circulation Model—Implementation and Simulation*

NING ZENG, J. DAVID NEELIN, AND CHIA CHOU

Department of Atmospheric Sciences and Institute of Geophysics and Planetary Physics, University of California, Los Angeles, Los Angeles, California

(Manuscript received 28 July 1998, in final form 20 May 1999)

ABSTRACT

The quasi-equilibrium tropical circulation model (QTCM1) is implemented and tested. The formulation, described by Neelin and Zeng, uses a Galerkin framework in the vertical, but with basis functions tailored to quasi-equilibrium deep convective physics via analytical solutions. QTCM1 retains a single vertical structure of temperature and humidity. For a balanced treatment of dynamics and subgrid-scale physics, a physics parameterization package of intermediate complexity is developed. This includes a linearized longwave radiation scheme, a simple cloud prediction method, simple shortwave radiation schemes, and an intermediate land surface model.

The simulated climatology has a reasonable spatial pattern and seasonal evolution of the tropical convergence zones, including over land regions. Outgoing longwave radiation and net surface heat flux both appear satisfactory. The Asian monsoon is slightly weak but depicts the northward progression of the monsoon onset, and a monsoon wind shear index exhibits interannual variability associated with observed SST that is similar to general circulation model (GCM) results. The extent and position of the main El Niño–Southern Oscillation rainfall anomalies are simulated, as well as a number of the observed tropical and subtropical teleconnections. The seasonal cycle and interannual variability of the Amazon water budget, including evapotranspiration, interception loss, and surface and subsurface runoff, illustrate reasonable simulation of the hydrologic cycle. Sensitivity studies on effects of topography, evaporation formulation, and land surface processes are also conducted. While the results are imperfect with respect to observations, many aspects are comparable to or better than GCMs of the previous generation. Considering the complexity of these simulated phenomena, the model is computationally light and easy to diagnose. It thus provides a useful tool filling the niche between GCMs and simpler models.

1. Introduction

In Neelin and Zeng (2000, NZ hereafter), a class of model for the tropical circulation is proposed. We refer to these as quasi-equilibrium tropical circulation models (QTCMs) because the formulation exploits the constraints placed on the flow by deep convection, as represented by quasi-equilibrium (QE) thermodynamic closures in the convective parameterization. In particular, the model presented in NZ uses a version of the Betts and Miller (1986, 1993) deep convection scheme, in which it is assumed that the ensemble effect of deep convection is to reduce a certain measure of convective available potential energy (CAPE). This tends to constrain the large-scale temperature profile and thus the baroclinic pressure gradients. Analytical solutions of the vertical structure of temperature and velocity for deep convective regions based on this were produced as part of an ongoing project, summarized in Neelin (1997, hereafter N97). The QTCM makes use of these analytical solutions as basis functions within the numerical model, an approach referred to as ‘‘tailored basis functions,’’ since the retained vertical structures are tailored to the dominant physics of interest.

A small hierarchy of QTCMs is anticipated, in which successively higher accuracy is obtained by retaining additional vertical structures, or embedding additional physics. In NZ the simplest QTCM is chosen that adequately simulates primary features of the tropical climatology. This is termed QTCM1 because it retains a single vertical structure for temperature and humidity. By its derivation, it is expected to give an accurate solution in deep convective regions (compared to, say, a GCM with Betts–Miller convection). Within one radius of deformation of deep convective regions, it should remain reasonably accurate, because temperature gradients are not large. At midlatitudes it is simply a highly truncated vertical representation, roughly equivalent to a two-layer model, since the Galerkin representation is tailored to tropical vertical structures.

---

* University of California, Los Angeles, Institute of Geophysics and Planetary Physics Contribution Number 5098.

Corresponding author address: Dr. Ning Zeng, Department of Atmospheric Sciences, University of California, Los Angeles, Los Angeles, CA 90095-1565.
E-mail: zeng@atmos.ucla.edu

To accompany this representation of dynamics, a radiation package is derived (after Chou and Neelin 1996; Chou 1997) that represents the main radiative processes at an intermediate level of complexity. This includes leading cloud–radiation interaction effects, since these are important to the general circulation, and since dynamics of convection zones is of interest. Likewise, a land surface model is presented that includes the essentials of more complex land surface models such as the biophysical control on evapotranspiration and surface hydrology but retains computational and diagnostic simplicity. The QTCM thus occupies a niche intermediate between GCMs and simpler models. It is related to GCMs in having a step-by-step derivation from the primitive equations, a convective parameterization based on parcel buoyancy considerations, and two-stream radiative schemes with cloud interaction, while remaining computationally efficient and simple to analyze. For instance, NZ discuss ways in which the moist static energy budget allows more direct access to fundamental dynamics in convection zones, especially over land regions. An example of testing the impact of a process by intervening in the model to suppress it is provided in Lin et al. (2000), in which the impact of midlatitude disturbances upon intraseasonal oscillations is tested.

The analysis of the equations and the preliminary results in NZ suggest that QTCM1 can potentially be useful for tropical studies. Here we provide a sampling of the simulation for a variety of phenomena. Implementation of cloud prediction, shortwave and longwave radiation schemes, and the land surface scheme is specified in section 2. Section 3 presents, in turn, the simulated climatology; sensitivity of this simulation to various parameterizations; the intraseasonal oscillation; interannual variability forced by observed SST, including El Niño–Southern Oscillation variability; the seasonal and interannual evolution of the Southeast Asian monsoon; and the Amazon water budget. Conclusions are provided in section 4.

2. Model description, implementation

a. Dynamics and convection

The detailed derivations and interpretations of the dynamics and moist convection in the model are discussed in NZ, and the main dynamic equations of QTCM1 are summarized in their section 5.

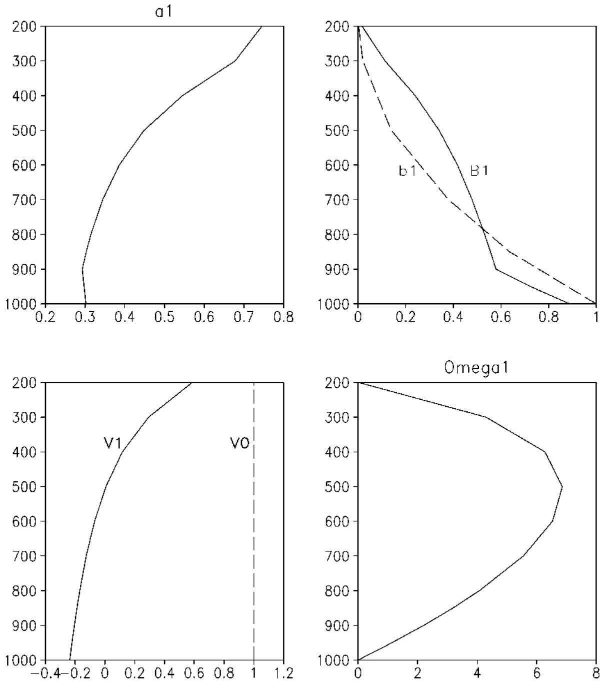

FIG. 1. Vertical profiles of basis functions for (a) temperature a_1, (b) moisture b_1 (dashed) and moisture convective reference profile B_1 (solid), (c) horizontal velocity V_1 and V_0, and (d) implied profile of vertical velocity Ω_1.

The model carries the amplitudes of the vertical structures of temperature T_1, humidity q_1, the baroclinic component of the horizontal velocity $\mathbf{v}_1$, and the barotropic component $\mathbf{v}_0$ (the barotropic vorticity is the actual prognostic variable) as the prognostic variables. Their vertical profiles are derived offline. These vertical profiles a_1, b_1, V_1, and V_0, as well as the profile for vertical velocity Ω_1, are shown in Fig. 1. Note that the baroclinic profile V_1 is not exactly symmetric about the midatmospheric level as assumed in simpler models (e.g., Gill 1980) but shows more subtle structure resulting from integrating the hydrostatic equation using the retained temperature profile. Since the vertical moisture structure in moist convective regions is less constrained (see NZ), we have more freedom in choosing the actual humidity profile b_1 such that it does not have to be the same as the fixed subsaturation moist adiabatic profile B_1.

Given the vertical profiles, the total fields can be reconstructed at any vertical level [see NZ Eqs. (3.6)–(3.8)] as

$$T = T_r(p) + a_1(p)T_1(x, y, t) \tag{2.1}$$

$$q = q_r(p) + b_1(p)q_1(x, y, t) \tag{2.2}$$

$$\mathbf{v} = \mathbf{v}_0(x, y, t) + V_1(p)\mathbf{v}_1(x, y, t), \tag{2.3}$$

where T_r and q_r are the reference profiles chosen to be typical for the tropical deep convective regions, x is longitude, y is latitude, and p is pressure. Note that the model predicts the total wind, while temperature and humidity are deviations from a reference profile.

b. Cloud prediction and radiation

The radiation scheme and cloud fraction parameterization presented here is modified for the QTCM from Chou and Neelin (1996) and an extension of Chou (1997). The cloud prediction scheme diagnostically estimates cloud fraction based on empirical formula. The longwave radiation scheme is adapted from Chou and Neelin (1996) to calculate upward and downward fluxes at the surface and upward fluxes at the top of the atmosphere. We offer three versions of the radiation package here: one with diurnal cycle, ‘‘clrad1-d’’; and two in which the solar component is diurnally averaged, clrad1 and clrad0. The clrad1 versions have a shortwave radiation scheme that is simplified from the Fu and Liou (1993) scheme for two components of solar radiation, surface solar irradiance and atmospheric column absorption. It is set up to include several cloud-cover types either predicted or specified from observation. The clrad0 version has a shortwave radiation scheme motivated by Kiehl (1992) and uses a combined cloud-cover type.

1) CLOUD PREDICTION

As shown in Chou (1997), four cloud types, deep cloud, cirrostratus–cirrocumulus (CsCc), cirrus, and stratus, as classified in the International Satellite Cloud Climatology Project (ISCCP) data (Rossow and Schiffer 1991) can capture 80% of the low-frequency variance in the radiation budget in the Tropics. For the QTCM, the primary concern is to simulate mean cloudiness averaged over weekly timescales and large spatial scales, rather than to simulate cloudiness variations at every time step. We also work with cloud cover types rather than the usual GCM level-by-level and prognostic approaches. Cloud cover types have a defined vertical structure, for instance, a deep convective tower accompanied by a fixed area of anvil.

Deep convection and associated clouds are important for the study of large-scale phenomena, such as the Madden–Julian oscillation and interannual variability, and have a fairly direct relationship to simulated large-scale variables, such as convective heating. Therefore, we parameterize the clouds associated with deep convection first. An empirical cloud prediction scheme for the high clouds associated with deep convection, including cloud clusters, is based on ISCCP C2 data. A linear relation between deep cloud and CsCc (the optically thicker type of cloud) is found, with ratio 1.01. This linear relation provides a simple parameterization that allows a substantial part of the high cloud to be combined with the deep cloud into a single cloud-cover type, which can be visualized as tower–anvil cloud, abbreviated as cloud type 1 hereafter. Of course, not all the high clouds included this way need be actual anvils, rather simply to have a close connection with the deep convective source. Next, combining the Xie–Arkin precipitation (Xie and Arkin 1996) with the ISCCP C2 data, a linear relation is found between the cloud fraction of cloud type 1 and precipitation. The coefficient is 7.76×10^{-4} $(\mathrm{W\ m^{-2}})^{-1}$ with precipitation in units of $\mathrm{W\ m^{-2}}$ ($1\ \mathrm{mm\ day^{-1}} = 28\ \mathrm{W\ m^{-2}}$). The parameterization of optically thinner high-layer cloud (cloud type 2), ‘‘cirrus’’ by the ISCCP C product definition, and stratus (cloud type 3) is ongoing work. For the current QTCM, the ISCCP monthly climatology is used as input for cloud types 2 and 3 in runs with clrad1. The impact of this in atmospheric dynamics is small, although it is important for surface fluxes. Experiments with clrad0 combine high and middle clouds as one single cloud type, whose amount depends on model precipitation; no cloud data is input for clrad0 runs.

2) LONGWAVE RADIATION SCHEME

Longwave radiation is derived from a simplified longwave radiation scheme (Chou and Neelin 1996) with the Green’s functions projected on the retained basis function in temperature and moisture. Because of this projection, only three components of longwave radiative fluxes, $R_t^{\downarrow}$, $R_s^{\uparrow}$, and $R_t^{\uparrow}$, are needed in the QTCM. The weakly nonlinear longwave radiation scheme coded in the packages of clrad1 and clrad1-d is

$$\begin{aligned} R_t^{\uparrow} &= R_{rt}^{\uparrow} + \sum_{n=0}^{N} \alpha_n [\epsilon_{RT_1t}^{\uparrow n} T_1 + \epsilon_{Rq_1t}^{\uparrow n} q_1 + \epsilon_{RT_st}^{\uparrow n}(T_s - T_{rs})] \\ &\quad + \sum_{n=1}^{N} \epsilon_{R\alpha_nt}^{\uparrow}(\alpha_n - \alpha_{rn}), \\ R_s^{\downarrow} &= R_{rs}^{\downarrow} + \sum_{n=0}^{N} \alpha_n [\epsilon_{RT_1s}^{\downarrow n} T_1 + \epsilon_{Rq_1s}^{\downarrow n} q_1] \\ &\quad + \sum_{n=1}^{N} \epsilon_{R\alpha_ns}^{\downarrow}(\alpha_n - \alpha_{rn}), \\ R_s^{\uparrow} &= R_{rs}^{\uparrow} + \epsilon_{RT_ss}^{\uparrow}(T_s - T_{rs}), \end{aligned} \tag{2.4}$$

where subscripts s and t denote surface and top, respectively; α_n and α_{rn} are cloud fraction and reference cloud fraction for cloud type n; and $n = 0$ represents clear sky. In (2.4), α_{rn} can be set to zero, and then $R_{rt}^{\uparrow}$ and $R_{rs}^{\downarrow}$ are the values for clear sky. Reference cloud fraction, α_{rn}, is used for consistency with the linear scheme [see NZ Eq. (4.45)]. Values for cloud types $n = 1$, 2, and 3, are $\alpha_{rn} = 0.11$, 0.10, and 0.12, respectively, in QTCM1 v2.1. Coefficients in the longwave scheme are precalculated as, for instance,

$$\epsilon_{Rq_1t}^{\uparrow n} = \int_{p_0}^{p_s} G_q^{\uparrow n}(p_t, \grave{p}) b_1(\grave{p})\, d\grave{p}, \tag{2.5}$$

with $G_q^{\uparrow n}$ obtained from the Harshvardhan et al. (1987) scheme, a full longwave radiation scheme. This scheme is not much more complex than a Newtonian cooling in formula but maintains the complexity of a full longwave radiation scheme in physics. The values of the coefficients for each cloud type are shown in Table 1.

Because of the specified cloud treatment, the cloud-top contribution to longwave radiation is relatively small (see Chou and Neelin 1996), so we neglect its effects here. For the linear version of this scheme (used in clrad0), cloud fraction is absorbed into the Green’s func-

TABLE 1. Parameters for the longwave radiation scheme from projecting Chou and Neelin (1996) Green's functions onto retained basis functions for clear sky ($n = 0$) and three cloud types ($n = 1, 2, 3$). See (2.1) and section 2b(2) for details. Units: W m^{-2} K^{-1} except $\epsilon^{\uparrow}_{R\alpha_n t}$ and $\epsilon^{\downarrow}_{R\alpha_n s}$, which are in W m^{-2} per cloud fraction change, which is unitless. The value of $\epsilon^{\uparrow}_{R\alpha_n s}$ is independent of cloudiness and so is listed with clear sky values.

Cloud type	$\epsilon^{\uparrow n}_{RT_1 t}$	$\epsilon^{\uparrow n}_{Rq_1 t}$	$\epsilon^{\uparrow n}_{RT_s t}$	$\epsilon^{\uparrow}_{R\alpha_n t}$	$\epsilon^{\downarrow n}_{RT_1 s}$	$\epsilon^{\downarrow n}_{Rq_1 s}$	$\epsilon^{\downarrow}_{R\alpha_n s}$	$\epsilon^{\uparrow}_{RT_s s}$
$n = 0$	1.335	−0.806	0.535		1.292	2.591		6.283
$n = 1$	1.529	-6.71×10^{-2}	3.04×10^{-3}	-1.004×10^{2}	1.757	0.635	24.809	
$n = 2$	1.454	−0.352	0.208	−61.689	1.518	1.731	8.432	
$n = 3$	1.409	−0.485	2.18×10^{-2}	−11.812	1.837	0.157	34.848	

tions [see Eq. (4.45) of NZ], so the linear scheme is computationally faster than the weakly nonlinear scheme with a little less accuracy (see Chou and Neelin 1996 for a comparison).

3) SHORTWAVE RADIATION SCHEME—CLRAD1 AND CLRAD1-D

Surface solar irradiance ($S^{\downarrow}_s$) and net solar absorption by the atmospheric column ($S^{\downarrow}_t - S^{\uparrow}_t - S^{\downarrow}_s + S^{\uparrow}_s$) are the primary components of shortwave radiative fluxes required in the QTCM equations during integration. The solar radiative fluxes mainly depend on solar zenith angle (θ) and surface albedo (A_s). The impact of variations of aerosol and atmospheric gases, such as ozone and CO$_2$, on the solar radiative fluxes are relatively small compared to the dependence on θ and A_s. Therefore, the first-order variation of the solar radiative fluxes can be approximated by simple formulas,

$$S^{\downarrow}_t - S^{\uparrow}_t - S^{\downarrow}_s + S^{\uparrow}_s = S_0 \cos\theta \sum_{n=0}^{N} \alpha_n f_{an}(\theta) g_{an}(A_s), \quad (2.6)$$

$$S^{\downarrow}_s = S_0 \cos\theta \sum_{n=0}^{N} \alpha_n f^{\downarrow}_{sn}(\theta) g^{\downarrow}_{sn}(A_s), \quad (2.7)$$

where S_0 is solar constant. Subscripts "a" indicate quantities associated with atmospheric absorption, and subscripts "s" indicate quantities associated with (downward) surface flux. Subscripts "n" indicate cloud type. To obtain the functions of $f_{an}(\theta)$, $g_{an}(A_s)$, $f^{\downarrow}_{sn}(\theta)$, and $g^{\downarrow}_{sn}(A_s)$, we use the Fu and Liou (1993) solar radiation scheme and input a typical vertical profile of water vapor, temperature, CO$_2$, ozone, and aerosol. We then use curve fitting to approximate these two functions for conditions with clear sky and with different cloud types. This stripped-down shortwave radiation scheme captures the first-order effects of radiative processes in the Fu and Liou scheme implicitly, for instance, multiple scattering between cloud base and the surface.

The QTCM focuses mainly on the Tropics, so the functions $f_{an}(\theta)$, $g_{an}(A_s)$, $f^{\downarrow}_{sn}(\theta)$, and $g^{\downarrow}_{sn}(A_s)$ can be simply written as

$$f_{an}(\theta) = a_{an} \cos\theta + b_{an},$$
$$f^{\downarrow}_{sn}(\theta) = a^{\downarrow}_{sn} \cos\theta + b^{\downarrow}_{sn},$$
$$g_{an}(A_s) = c_{an} A_s, \qquad g^{\downarrow}_{sn}(A_s) = c^{\downarrow}_{sn} A_s, \quad (2.8)$$

where a_{an}, b_{an}, c_{an}, $a^{\downarrow}_{sn}$, $b^{\downarrow}_{sn}$, and $c^{\downarrow}_{sn}$ are constant, with values given in Table 2. These approximations are accurate for low surface albedo ($A_s < 0.6$) and low solar zenith angle ($\cos\theta > 0.4$). In the QTCM, the cloud prediction scheme is designed for longer timescales and larger spatial scales, so for consistency, the radiative fluxes are diurnally averaged before interacting with clouds in the standard version of radiation code (clrad1). This is done by analytical averaging of (2.6)–(2.8); the diurnal average of $\cos\theta$ and $\cos^2\theta$ that result are

$$\overline{\cos\theta}^{\text{day}} = 1/\pi(H \sin\lambda \sin\delta + \cos\lambda \cos\delta \sin H) \quad (2.9)$$

$$\begin{aligned}\overline{\cos^2\theta}^{\text{day}} = {} & 1/\pi[H \sin^2\lambda \sin^2\delta \\ & + 2 \sin\lambda \cos\lambda \sin\delta \cos\delta \sin H \\ & + \cos^2\lambda \cos^2\delta(H/2 + \sin 2H/4)], \end{aligned} \quad (2.10)$$

where λ is the latitude and δ is the solar declination. The quantity $H = \cos^{-1}(-\tan\lambda \tan\delta)$ represents the half-day, from sunrise or sunset to solar noon (Liou 1980). A version with diurnal cycle also is included for examination of diurnal effects. Surface albedo in the current QTCM is a monthly climatology derived from Darnell et al. (1992) that is consistent with the Earth Radiation Budget Experiment data.

TABLE 2. Parameters for the clrad1 shortwave radiation scheme from the fitting of (2.6)–(2.8) to the Fu and Liou (1993) solar scheme, for clear sky ($n = 0$) and three cloud types. Values are unitless.

Cloud type	$a^{\downarrow}_{sn}$	$b^{\downarrow}_{sn}$	$c^{\downarrow}_{sn}$	a_{an}	b_{an}	c_{an}
$n = 0$	-6.992×10^{-2}	0.249	0.166	0.134	0.646	7.898×10^{-2}
$n = 1$	2.862×10^{-2}	0.176	6.384×10^{-2}	0.148	8.236×10^{-2}	0.744
$n = 2$	-3.275×10^{-2}	0.218	0.176	0.295	0.386	0.255
$n = 3$	-3.075×10^{-2}	0.260	6.907×10^{-2}	0.285	0.150	0.580

TABLE 3. Parameter values used in the land surface model [consolidated from the Biosphere–Atmosphere Transfer Scheme (BATS) and the Simple Biosphere 2 scheme (SIB2; Sellers et al. 1996)]. The listed albedo values are not used in the standard version of QTCM1; see text for details.

Parameter	Ocean	Forest	Grass	Desert
Surface albedo A_s	0.07	0.12	0.19	0.3
Min resistance $r_{s\,min}$ (m^{-1} s)		150	200	200
Field capacity W_0 (mm)		500	400	300
Roughness length Z_0 (m)	0.0024	2.0	0.1	0.05
Leaf area index		6	3	1

4) SHORTWAVE RADIATION SCHEME—CLRAD0

A simpler shortwave radiation scheme is also provided for use in QTCM1. The scheme clrad0 assumes highly simplified physics, but the assumptions are more transparent. Following Kiehl (1992) and Zeng and Neelin (1999), the scheme assumes a single layer of cloud/atmosphere with a lumped reflectivity A_c (including contributions from clouds, aerosol, and atmospheric backscattering) and absorptivity a_{bs} (including contributions from water vapor, clouds, etc.). A single cloud type combines high and middle clouds, and the cloud cover is proportional to the model precipitation [section 2b(1)]. Given a surface albedo A_s, one can derive the fluxes at surface and top (see Zeng and Neelin 1999 for details). For instance, the downward flux at the surface and upward flux at the top are

$$S_s^{\downarrow} = (1 - A_c)(1 - a_{bs})S_0 \cos\theta \tag{2.11}$$

$$S_t^{\uparrow} = [(1 - A_c)^2(1 - a_{bs})^2 A_s + A_c]S_0 \cos\theta. \tag{2.12}$$

A diurnally averaged solar zenith angle dependence has been absorbed in A_c and a_{bs}.

c. Surface fluxes

The surface fluxes are parameterized using the bulk transfer formulas following Deardorff (1972). These include momentum flux (stress) τ_s, evaporation E, and sensible heat flux H:

$$\tau_s = \rho_a C_D \mathrm{V}_s \mathbf{v}_s \tag{2.13}$$

$$E = \rho_a C_H \mathrm{V}_s [q_{sat}(T_s) - q_a] \tag{2.14}$$

$$H = C_p \rho_a C_H \mathrm{V}_s (T_s - T_a), \tag{2.15}$$

where ρ_a is the near-surface air density; C_p is the specific heat at constant pressure; $\mathbf{v}_s$ is the surface wind velocity; T_s is the surface temperature (SST over ocean, ground temperature over land), $q_{sat}(T_s)$ is the saturation humidity at T_s; T_a and q_a are the surface air temperature and humidity reconstructed using (2.1) and (2.2), respectively; and C_D and C_H are a surface roughness–dependent drag coefficients and C_D has a value of 1.0×10^{-3} over ocean (see Table 3 for surface type–dependent parameter values). The current version of the model does not attempt to predict the boundary layer depth and stability, so C_D is the neutral value calculated using Deardorff's formulation for a 2-km deep boundary layer:

$$C_D = \left[k^{-1} \ln\left(\frac{0.025 z_B}{z_0}\right) + 8.4\right]^{-2}, \tag{2.16}$$

where z_B is the boundary layer depth, z_0 is the roughness length, and $k = 0.4$ is the von Kármán constant. For results shown here, the approximation $C_H = C_D$ is used. The ''effective'' magnitude of the surface wind speed V_s is parameterized as

$$\mathrm{V}_s^2 = \mathrm{V}_{s_{min}}^2 + |\eta \mathbf{v}_s|^2, \tag{2.17}$$

where $V_{s_{min}}$ is a minimum wind speed that accounts for wind variations at scales not resolved by the model (Esbensen and McPhaden 1996). Since the current version of QTCM lacks an explicit boundary layer (see NZ), the actual wind speed predicted by the model $\mathbf{v}_s$ in (2.17) is reduced by a factor η. This mimics an extrapolation from the free atmosphere into the boundary layer based on empirical relationships (e.g., Garratt 1992). In the standard version, η is taken to be 0.6 and $V_{s_{min}}$ is taken to be 5 m s^{-1}. GCM simulations are sensitive to evaporation formulation (e.g., Palmer et al. 1992). Similar sensitivities are found in our model. An example of this is given in section 3c. Equation (2.14) is used only over ocean. A surface resistance parameterization of evaporation is used over land (see below).

d. Land surface model

Recent land surface models tend to be complex and contain detailed parameterizations of surface hydrology and plant physiology aimed at many hydrological and biological applications (e.g., Dickinson et al. 1993; Sellers et al. 1996). On the other hand, the much simpler single-layer bucket model (Budyko 1974; Manabe et al. 1965) has been widely studied and proves a powerful diagnostic tool (e.g., Delworth and Manabe 1993). However, the bucket model tends to overestimate initial evaporation and can lead to overly dry soil because of the lack of vegetation control. The main missing factor for the bucket model is the stomatal resistance (Sato et al. 1989). In simple to intermediate models, simple, and sometimes rather arbitrary, assumptions are made in land surface parameterizations.

Here we develop a land surface parameterization scheme of intermediate complexity that models the first-order effects relevant to climate simulation, while from a diagnostic and computational point of view, it is only moderately more complicated than the bucket model. It is termed simple-land, abbreviated ''SLand.'' It does not attempt to resolve accurately the diurnal solar and environmental control on photosynthesis. Thus, the soil moisture and seasonal variation of radiation are the main controlling factors. The most essential features for climate simulation are the low heat capacity of the land surface and specification of land albedo for the surface energy budget, and soil moisture and its consequences for the surface water budget. Subgrid-scale variability of rainfall can significantly influence surface runoff and interception loss and therefore evaporation. Various analytical formulations have been proposed (e.g., Entekhabi and Eagleson 1989). We follow a similar statistical approach but with choices in line with the level of complexity of our atmospheric model.

In SLand, a single soil layer is assumed but with different depth for the energy and the water balance. For the energy balance, it essentially models the top soil layer with a typical thickness of 10 cm. The prognostic equation for ground temperature T_s is

$$C_s \frac{\partial T_s}{\partial t} = F_s^{\mathrm{rad}} - E - H, \tag{2.18}$$

where C_s is the soil heat capacity, $F_s^{\mathrm{rad}} = S_s^{\downarrow} - S_s^{\uparrow} + R_s^{\downarrow} - R_s^{\uparrow}$ is downward net radiation at surface, E is the total evaporation, and H is the sensible heat flux. A small heat capacity C_s leads to a damping timescale on the order of 1 h, so on timescales longer than a day, one has $F_s^{\mathrm{rad}} - E - H \approx 0$. This flux zero condition has been used explicitly by some early GCMs, and it imposes arguably the most important control on land surface–atmosphere interaction (Zeng and Neelin 1999; NZ).

The water budget equation in a single soil layer that represents the root zone is

$$\frac{\partial W}{\partial t} = P - E_I - R_s - E_T - R_g, \tag{2.19}$$

where W is the soil moisture content per unit area and P is the precipitation. The soil is saturated when W equals the field capacity W_0, which is surface type dependent. It is useful to define a relative soil wetness,

$$w = W/W_0, \tag{2.20}$$

such that w is unity at saturation. The total evaporation can be expressed as the sum of the interception loss E_I and the evapotranspiration E_T:

$$E = E_I + E_T. \tag{2.21}$$

The total runoff R is the sum of surface runoff R_s (the fast component) and subsurface runoff R_g (the slow component):

$$R = R_s + R_g. \tag{2.22}$$

The order of the terms on the rhs of (2.19) is nontrivial because it represents the approximate timing of the occurrence of the processes, as the intercepted water is not available for surface runoff, and neither of them is available for evapotranspiration and subsurface runoff.

For the water sinks, we first write down general forms that functionally encompass what have been used in the current land surface schemes (e.g., Shao and Henderson-Sellers 1996). For interception loss:

$$E_I = E_I(P, F_s^{\mathrm{rad}}). \tag{2.23}$$

The intercepted water is not available for surface runoff:

$$R_s = \gamma_s(w)(P - E_I), \tag{2.24}$$

and subsurface runoff is

$$R_g = \gamma_g(w) R_{g0}, \tag{2.25}$$

where R_{g0} is the subsurface runoff at saturation, $\gamma_s(w)$ and $\gamma_g(w)$ are nonlinear functions of w to be specified. For evapotranspiration:

$$E_T = (r_s + r_a)^{-1} \rho_a [q_{\mathrm{sat}}(T_s) - q_a], \tag{2.26}$$

where $r_a = (C_D V_s)^{-1}$ is the aerodynamic resistance, r_s is a bulk surface resistance including stomatal/root resistance parameterized as

$$r_s = \frac{r_{s_{\min}}}{\beta(w)}, \tag{2.27}$$

where $r_{s_{\min}}$ is the minimum value of r_s occurring at no water stress ($\beta = 1$), and β is specified below.

A main objective of SLand is to model the land surface fluxes at large spatial and long temporal scales by statistically taking into account smaller and faster scale variations. In the above parameterizations the dependent variables are w, F_s^{rad}, and P. The scaling used in the parameterizations is such that the dimensionless soil wetness–dependent functions $\beta(w)$, $\gamma_s(w)$, and $\gamma_g(w)$ range from 0 to 1 (for w ranging from 0 to 1) and can be highly nonlinear. These functions lump the effects of temporal and spatial variability of rainfall and surface characteristics, including potentially important factors like soil infiltration capacity (Lean et al. 1996). They can be specified following the ‘‘semiempirical’’ formulations of Koster and Milly (1997) or more physically based parameterizations such as Entekhabi and Eagleson (1989). In the current version of the model, we use the following parameterizations:

$$\gamma_s = w^4 \tag{2.28}$$

$$\gamma_g = w^{2B+3} \tag{2.29}$$

$$\beta = w^{1/4}, \tag{2.30}$$

where B is the Clapp–Hornberger exponent. The parameterizations for γ_s and γ_g are essentially the formulations used in the Biosphere–Atmosphere Transfer Scheme (Dickinson et al. 1993). The nonlinear dependence of β on w takes into account effects of the soil moisture uptake by deep roots under relatively dry conditions such as what happens during the Amazon dry season (Shuttleworth 1988). The actual form of β is chosen in accordance with observations (e.g., Bras 1990) and physically based parameterizations including heterogeneity effects (e.g., Entekhabi and Eagleson 1989). The interception loss formulation used in the current model version takes into account the spatiotemporal variability of rainfall following Zeng et al. (2000b):

$$E_I = E_{I0}F(P,\ \tau_a,\ \tau_r,\ \tau_0), \tag{2.31}$$

where E_{I0} is the potential evaporation for intercepted water, F is an interception function depending on model simulated precipitation P, τ_a is the prescribed mean interstorm arrival time, storm duration τ_r based on observed convective rainfall, and τ_0 is the time to evaporate a saturated canopy at potential rate (i.e., E_{I0}), which depends on the leaf area index. E_{I0} is taken to be the available energy F_s^{rad} in conjunction with a simple atmospheric model like QTCM1, although it tends to be somewhat larger than net radiation in observations (Zeng et al. 2000b).

The model SLand differs from the bucket model primarily in its parameterization of evapotranspiration processes. In (2.26) the surface resistance r_s (more than 100 m^{-1} s; Table 3) is typically much larger than r_a (about 10 m^{-1} s for forest), so that (2.26) can be rearranged into a form similar to the bucket model:

$$E_T \approx \beta \frac{r_a}{r_{s_{\min}}} \rho_a C_D \mathrm{V}_s[q_{\mathrm{sat}}(T_s) - q_a]. \tag{2.32}$$

It is both conceptually and diagnostically convenient to define a potential evaporation that is the evaporation at no water stress ($\beta = 1$):

$$\begin{aligned} E_p &= (r_{s_{\min}} + r_a)^{-1}\rho_a[q_{\mathrm{sat}}(T_s) - q_a] \\ &\approx \frac{r_a}{r_{s_{\min}}}\rho_a C_D \mathrm{V}_s[q_{\mathrm{sat}}(T_s) - q_a], \end{aligned} \tag{2.33}$$

such that

$$E_T \approx \beta E_p. \tag{2.34}$$

Besides the difference in specifying $\beta(w)$ (a linear dependence on w is used in the bucket model), the most significant difference between (2.32) or (2.33) and the bucket model is that the transfer coefficient is reduced by a factor $r_a/r_{s_{\min}}$ as the potential evaporation is limited by vegetation control, in addition to the aerodynamic resistance. The parameterization used here avoids the most severe problem in the original bucket model in a physically realistic way, while retaining much of its conceptual simplicity and diagnostic power.

Although the scheme allows many land surface types as long as the relevant parameter values are provided, we opt for a simple classification in the standard version with three surface types: forest, grass, and desert, while more surface types can be used in applications emphasizing land surface processes. The most important surface properties include surface albedo and field capacity, which play critical roles in the energy and the water balance, respectively. The important surface type–dependent parameter values, including albedo, minimum surface resistance, field capacity, surface roughness, and leaf area index, are listed in Table 3. In the standard version of QTCM1, we use prescribed surface albedo derived from satellite observations (Darnell et al. 1992), while one can easily switch to using the surface albedos linked to surface type listed in Table 3. Sensitivity studies show discernible differences at regional scales between the two methods, but these have little impact on the global patterns. Snow hydrology is not simulated in this version, since the atmospheric model is aimed at the Tropics.

e. *Implementation*

The standard version of QTCM1 includes full nonlinearities in advection, convection, and land surface processes. Clouds associated with deep convection are predicted as one combined cloud type based on a simple precipitation–cloud-cover relationship (section 2b). In the radiation package clrad1, the climatological monthly means of stratocumulus and cirrus clouds are prescribed from observations, while the tropical mean of middle clouds is used (constant in space and time). In the simpler package clrad0, the tropical mean of low clouds is used while high and middle clouds are predicted as one lumped cloud type according to the model precipitation. The linearized longwave radiation scheme is used in clrad0, while clrad1 uses the weakly nonlinear version. Sensitivity studies (section 3c) show some differences between the two packages, but the overall behaviors are similar. The radiation packages are used with diurnally averaged incoming solar radiation, although diurnal cycle can be included as an option. The topographic effects on the barotropic vorticity equation are turned off in the standard version. A sensitivity study of this is shown in section 3c. Depending on the target phenomenon under study, one may wish to use different options, for example, the radiation package option. The coding of the model is modularized and sufficiently transparent that this is relatively easy.

The model domain covers the whole Tropics in longitude and extends to 60°N and 60°S in latitude. A sponge boundary is applied outside 45° latitude that involves a relaxation toward the Reynolds–Smith interpolated temperature over land and a damping of the heat and momentum flux. Some sensitivity to the strength of the sponge is seen in midlatitudes, with some impact in the subtropics but not much in the tropical climate. A horizontal grid spacing of 5.625° by 3.75° is used here. Selected results from the following sections have been tested at doubled resolution (in both latitude and longitude), without major changes. The prognostic equations are finite differenced on an Arakawa-C grid. The baroclinic component is similar to a shallow-water equation and is solved by applying a forward–backward scheme using the updated variables immediately. The barotropic component is solved in a vorticity–streamfunction formulation using an Adams–Bashforth scheme. The numerical CFL instability criterion limits the model time step at about 20 min, mostly due to the momentum advection associated with midlatitude baroclinic waves. On a Sun/Ultra2 workstation, it takes less than 5 min CPU time per year of simulation.

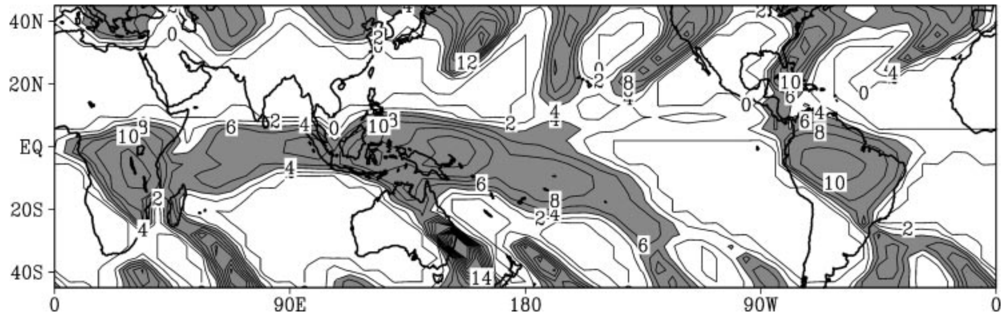

FIG. 2. Daily precipitation on a typical day (13 Jan) from the climatological SST run, showing the extratropical storms and tropical convergence zones. Contour interval 2 mm day^{-1}, shaded above 4 mm day^{-1}.

3. Model results

a. Overview

Results presented in this section come from two types of runs that differ only in the prescribed SST boundary condition: (i) 1982–98 runs driven by the observed SST of Reynolds and Smith (1994); monthly mean output from these runs is used to analyze the climatology and interannual variability; and (ii) seasonal runs driven by climatological SST; daily mean output is used in the analyses of intraseasonal oscillation and the seasonal evolution of the monsoon. Both use diurnally averaged solar radiation input. In addition, sensitivity studies (section 3c) are conducted using similar runs but with different options for the physics.

The presence of temperature advection and the baroclinic and barotropic wind components in velocity (similar to a two-layer model in terms of degrees of freedom) leads to baroclinic instability. Figure 2 depicts the daily rainfall for 13 January from the climatological SST run, showing the storms in the midlatitudes of both hemispheres. Zonal wavenumbers from 5 to 11 have the greatest power, especially wavenumbers 7 and 8. The strongest storms in this season occur in the winter North Pacific and North Atlantic. Detailed analysis indicates that the storms are somewhat too regular.

While the model Tropics does have intraseasonal variability (section 3d), it lacks mesoscale phenomena and is relatively steady compared to storm-related variations in midlatitudes. As evident in the Southern Hemisphere in Fig. 2, the ''tails'' of storms penetrate into the tropical convergence zones and can contribute to tropical variance. These connections tend to occur at preferred locations, and this effect appears to play a role in forming the climatological southern convergence zones (Fig. 3), namely, the South Pacific Convergence Zone (SPCZ), the South Atlantic Convergence Zone (SACZ), and a similar feature in the South Indian Ocean. In January climatology, these southern convergence zones emanate from the tropical convergence centers: the West Pacific warm pool, the Amazon, and equatorial Africa, similar to the observations (Fig. 4). There is also a smaller version of such a convergence zone over northeastern Australia although weaker than the SPCZ. A hint of its counterpart in the observation is seen as an intensification of the SPCZ over northern Australia with extension toward New Zealand. In observations, these southeastward extensions of the convergence zones are generally quite broad, whereas the model appears to have narrower versions of these.

The storms play an important role in drying the subtropics and feeding the moisture to midlatitudes. The storms appear to organize themselves somewhat in the North Pacific and North Atlantic, albeit not at realistic locations, likely due to the lack of topographic effects (see sensitivity study in section 3c). In places, the subtropical dry zones are a little too wide, and the storms too far poleward. The subtropical high-pressure regions such as in the southeastern Pacific appear to be slightly too dry and extend too far east such that southern South America is too dry. This is also partly responsible for the narrowness of the southeastern extensions of the convergence zones discussed above. For a model of this level of complexity aimed at tropical climate simulation, we do not expect a perfect simulation of midlatitude storms. Major effects relevant to the Tropics are the eddy flux of moisture, which dries the subtropics, and the eddy flux of momentum, which maintains the tropical zonal mean easterlies as discussed in NZ. The link between the subtropical and tropical convergence zones also appears relevant to teleconnections of climate anomalies. Overall, the results here seem very encouraging. We now shift our attention to the seasonal cycle of the rainfall patterns (Fig. 3, corresponding observations in Fig. 4).

In January, the major convective band runs over most of the equatorial Tropics, including the western Pacific warm pool region, the Amazon, Central Africa, and the Indian Ocean. However, parts of the ITCZ in the eastern Pacific and Atlantic are too weak. Sensitivity studies show that these features are sensitive to the parameterization of surface fluxes. The present version also lacks a separate explicit boundary layer that is thought to be important in maintaining the strength of these narrow convergence zones (Wang and Li 1993). As the sun moves northward, the equatorial convergence band also

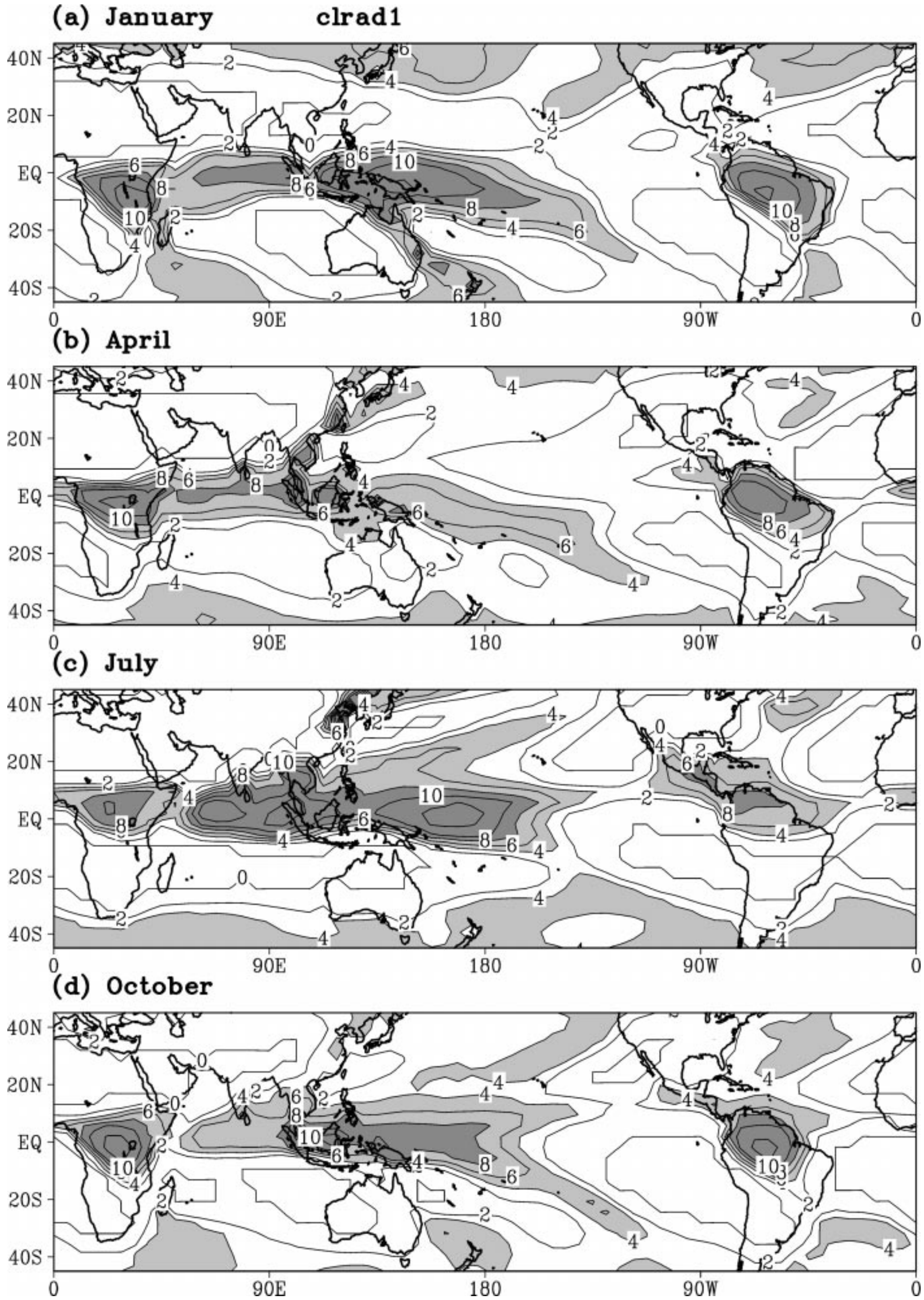

FIG. 3. Model climatological monthly mean precipitation for the period 1982–98; using the cloud–radiation package clrad1. (a) Jan, (b) Apr, (c) Jul, (d) Oct. Contour interval 2 mm day^{-1}, shaded above 4 mm day^{-1}.

moves northward from January to July. The ITCZ over the eastern Pacific and the Atlantic strengthens. Many detailed features are also captured by the model, such as the wet region around Madagascar, and the mid-Pacific trough near Hawaii. Throughout a seasonal cycle, rainfall over the Amazon basin is reasonable (see further discussion in section 3g), although the southward movement of the convergence zone occurs too early so that October has too much precipitation. Rainfall over Africa appears to be too strong all year round.

In April, the southern convergence zones become weaker, and the African monsoon has already started. The rainy season over northeastern Brazil is captured, as the ITCZ moves south. The seasonal cycle of rainfall in this region is generally reasonable; the rain begins in December/January (a bit early), is strong in April,

(a) January OBS

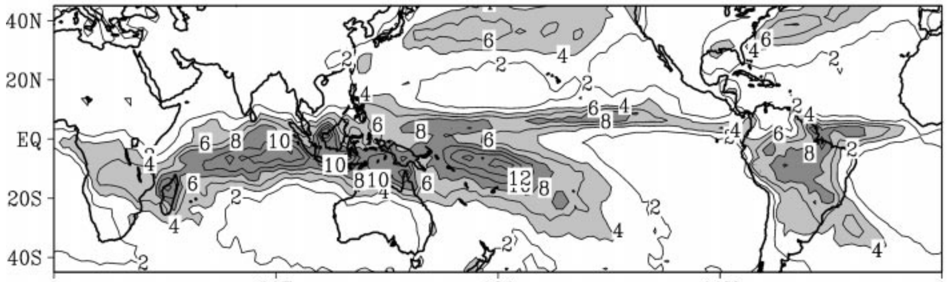

(b) April

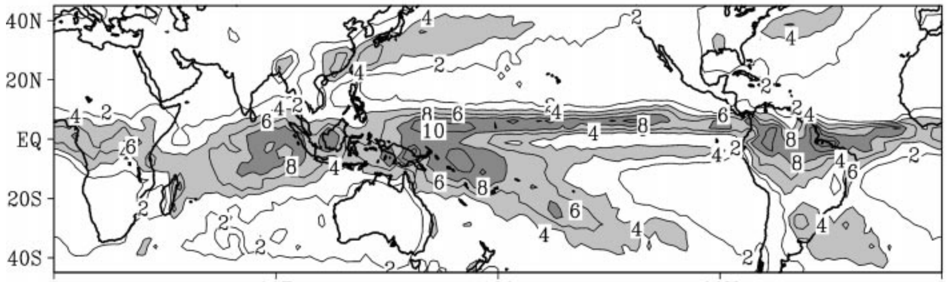

(c) July

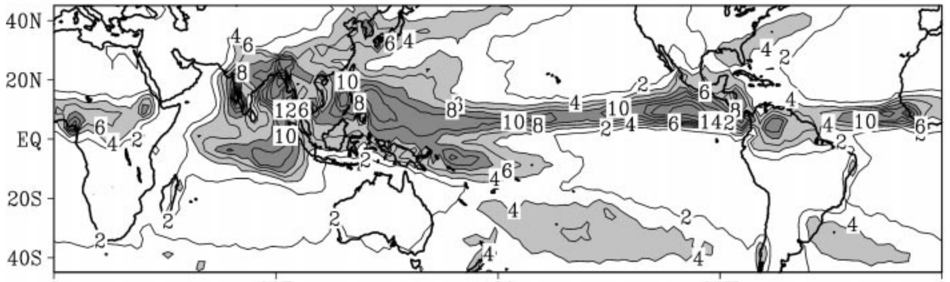

(d) October

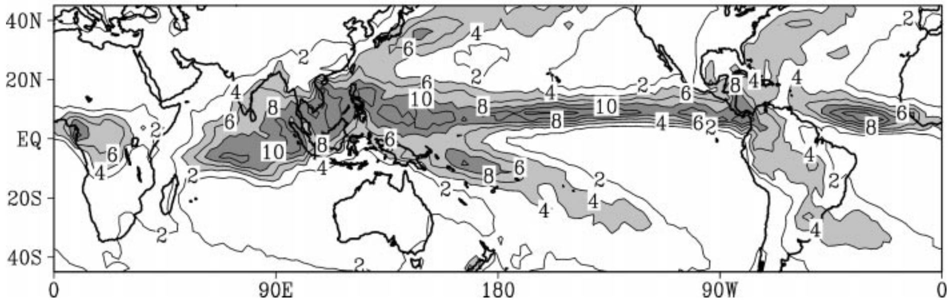

FIG. 4. As in Fig. 3, but from the observed Xie–Arkin precipitation.

and June through November are dry. This feature is quite sensitive to model parameters, and a small change in the ''notch'' between the Atlantic ITCZ and the South American convergence zone can affect it. In the current version the rainy season is long; an earlier version (QTCM1 version 2.0; Zeng et al. 2000a) did somewhat better in this region.

In July (Fig. 3c), the African and North American monsoons are well established. The largely zonal monsoon rain in west Africa extends from the rainforest into the Sahel at about 15°N. The northern boundary of this rainfall is quite successfully simulated, compared to a number of GCMs that tend to have rain encroaching into the Sahara. A wet tongue extends from Central America along the Pacific coast into Mexico and the southwest United States. The patterns and locations are similar to the observation (Fig. 4c). In the Asian monsoon region, India and southeast and east Asia receive large amount of monsoon rainfall, but southern China appears to have too little rainfall. Overall, the Asian monsoon appears to be too weak, especially in contrast with the unrealistically large maximum rainfall sitting over the equatorial Indian Ocean. A maximum over the Bay of Bengal is missing in the model. Another unrealistic feature is a large maximum around the date line. A similar tendency has been noted in some runs of the University of California, Los Angeles (UCLA), atmospheric general circulation model (C. R. Mechoso 1998, personal communication). This is shifted westward if evaporation parameterization is modified (section 3c). A band of rainfall emanating from this maximum toward the northeast bears a resemblance to the southern convergence zones in January. It is tempting to call this the Northern Pacific Convergence Zone (E. M. Rasmusson 1997, personal communication), although it is not exactly at the right location due to the mislocation of the date line maximum and lack of topography in the model. In October, the equatorial convergence centers have shifted back southward, and the southern convergence zones start to strengthen, although they remain somewhat too weak compared to the observation.

Overall, the model simulates a reasonable seasonal migration of tropical and subtropical convective rainfall centers. The African and American monsoons are well simulated, but the rainfall over the Indian Ocean and Pacific Ocean is concentrated too much along the equator. Correspondingly, the Asian monsoon appears somewhat weak. This suggests that the warmed continent in the model is able to shift the overall circulation, but not enough in the case of the Asian monsoon where other factors such as topography also play important roles. Further sensitivity studies are discussed in section 3c.

b. More on the climatology

Having seen an overview of the climatology in terms of precipitation, we now examine various other fields. Figure 5 depicts the January climatology of evaporation, outgoing longwave radiation (OLR), and net downward energy flux at the surface, compared to observations in Fig. 6. These fields are representative of the behavior of the model's physics packages, especially surface fluxes, cloud, and radiation.

Over the tropical oceans, the evaporation (Fig. 5a) pattern is determined mostly by SST and surface wind speed. The SST dependence is seen in the contrast between, say, the western Pacific warm pool and the cold tongue region. The wind speed dependence is apparent in the trade wind regions such as the North and South Pacific in the subtropics. Similar to the observations, the warm pool also has a local minimum due to the weak winds there. Experiments show that the evaporation in the weak wind region depends critically on the minimum wind $V_{s_{\min}}$ in (2.17), which represents sub-Reynolds-scale wind variability. The overall pattern and magnitude of evaporation are similar to the observations. Evaporation increases associated with midlatitude storm tracks are simulated, but not to the degree seen in observations (Fig. 6a), especially off the coast of east Asia. This is significantly improved in the version with topographic effects included (section 3c) where storm tracks are better located. Over land, the evaporation tends to follow precipitation but lasts longer into the dry season due to the soil moisture memory (see sections 3f, 3g), so that the pattern of evaporation is generally smoother than that of precipitation.

The model captures the pattern of low OLR (Fig. 5b) associated with tropical convergence zones due to the longwave trapping effects of the deep convective clouds, which are predicted according to precipitation in the model. Minimum values of about 230 W m^{-2} are seen in the warm pool region and over the Amazon, about 20–30 W m^{-2} too large compared to the observations in Fig. 6b (see section 3c for sensitivity to a different radiation package). As in the observations, the OLR increases toward the dry subtropics and decreases again at midlatitudes due to the presence of clouds and colder temperature. The subtropical OLR is quite reasonable, although a dry bias results in slightly low greenhouse trapping.

The net surface flux F_s (Fig. 5c) is the sum of the net radiation, evaporation, and the sensible heat flux. It is nearly zero over land at climate scales due to the low heat capacity of land (section 2d). Over ocean this quantity is important for coupling to ocean models. The simulated pattern is largely similar to the observations (Fig. 6c), exhibiting a gross seasonal contrast between the two hemispheres. In the Tropics, this gradient is significantly modified by the circulation patterns. The SPCZ has a strong signature as can be seen by tracing, say, the 50 W m^{-2} contour line. The warm pool region has small net flux. A 20–30 W m^{-2} difference can be easily seen in the Tropics between Fig. 5c and Fig. 6c, which is typical of the uncertainty in the observations (compare Fig. 6c with Hurrell et al. 1993). In the subtropical high regions, the net flux is reasonable. Near the eastern side of the ocean basins, it must be borne in mind that stratus is specified, which aids the simulation by reflecting more solar radiation into space. The fluxes under the storm tracks are captured, though somewhat underestimated.

Figure 7 depicts the model 850- and 300-mb winds [reconstructed according to Eq. (2.3)]. At 850 mb, the model simulates trade winds blowing across the subtropics. The trades are especially strong in the winter Northern Hemisphere. Midlatitude westerlies develop associated with the storms. The anticyclonic motions around the subtropical highs are well simulated, especially in the Southern Hemisphere. The winds turn southeastward correctly over the Amazon basin despite the lack of topography, suggesting that this is mostly a thermodynamical feature rather than a topographic one. Equatorial westerlies are also seen over Africa and the

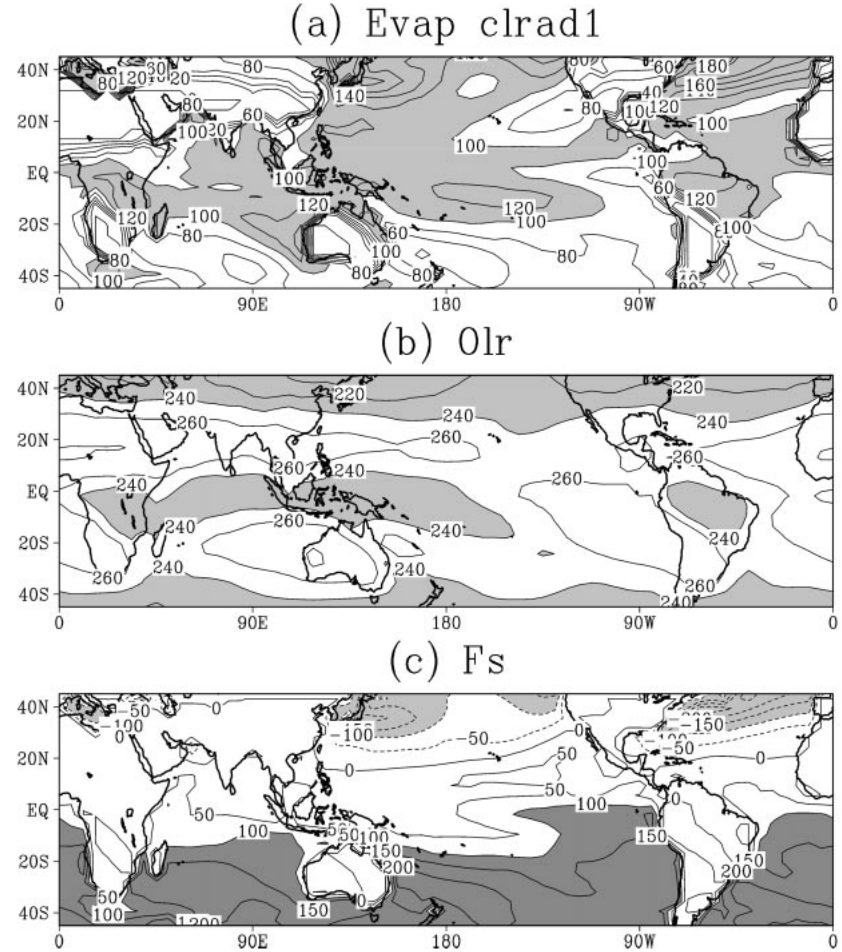

FIG. 5. Model-simulated Jan fluxes of (a) evaporation, contour interval 20 W m^{-2} and shaded above 100; (b) outgoing longwave radiation, contour interval 20 W m^{-2} and shaded below 240; (c) downward net surface energy flux F_s^{net}, contour interval 50 W m^{-2} with dark shading above 100 and light shading below -100 W m^{-1}.

.

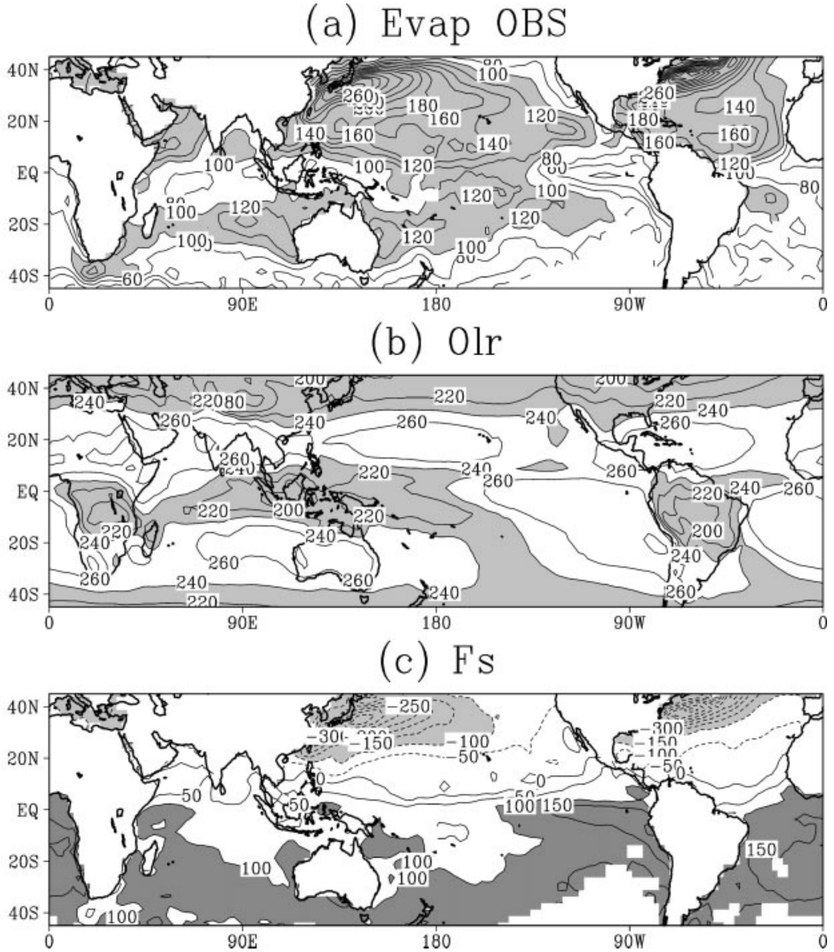

FIG. 6. As in Fig. 5, but for observations. The observed evaporation is from Oberhuber (1988); OLR is from the National Oceanic and Atmospheric Administration Climate Analysis Center; and the surface net flux is derived from Oberhuber's evaporation and sensible heat and the surface radiation budget of Darnell et al. (1992)

(a) 850 mb

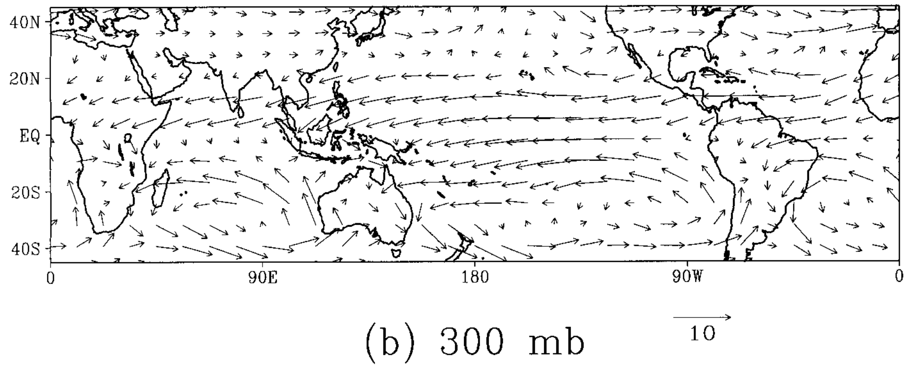

(b) 300 mb

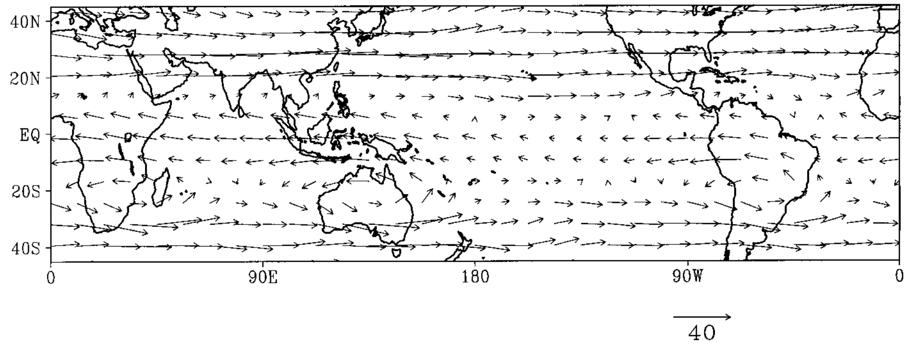

FIG. 7. Model-simulated Jan climatological winds at (a) 850, (b) 300 mb. (In m s^{-1}.)

Indonesian region, but they are not strong enough over the Indian Ocean.

The 300-mb (Fig. 7b) winds are dominated by the subtropical westerly jets. The Northern Hemisphere jet is located at about 30°N, similar to observations, but the Southern Hemisphere jet is somewhat too close to the equator. Both jets are slightly too strong. The Tropics are dominated by the easterlies with a hint of change to westerlies in the so-called westerly duct region in the eastern Pacific, although not as strongly westerly as in the observations.

The zonal average zonal velocity is similar to what is shown in Fig. 4 of NZ. The Northern Hemisphere trades are centered at about 15°N, similar to the observations from the National Center for Environmental Prediction–National Center for Atmospheric Research (NCEP–NCAR) reanalysis (Kalnay et al. 1996). The subtropical jets are somewhat too strong, and the easterlies extend slightly too far poleward. These correspond to a slightly too high wind shear at midlatitudes in the baroclinic mode, which is derived from a tropical moist adiabat profile by design. Overall, given the limited degrees of freedom, the model-simulated wind field is quite encouraging.

The July climatology of the atmospheric temperature averaged between 500 and 200 mb [reconstructed using (2.1)], surface temperature, soil wetness, and 850-mb winds are shown in Fig.8. The atmospheric temperature at 500–200 mb is chosen so that a direct comparison with the observation of Li and Yanai (1996, Fig. 3) can be made. The most prominent feature in Fig. 8a is the warm temperature center around the Tibetan Plateau, corresponding to high pressure aloft and low pressure at low levels for the baroclinic component. Careful examination indicates that this monsoon depression is located slightly too far west of the Tibetan Plateau (which does not exist in this model run). At 850 mb, the southwesterly winds over the Indian Ocean turn around this monsoon depression and then join the trade winds from the western Pacific, flowing northward into the eastern Asian trough (Fig. 8d). Over North America, a temperature ridge has developed associated with the North American monsoon.

As an indication of the land surface model's performance, the July surface temperature T_s is shown (Fig. 8b; it is just the observed SST over ocean). It is high in the Northern Hemisphere continents; in regions, somewhat too high, even allowing for lack of topography, likely due to errors in the model energy balance and lack of a deep soil layer. Interestingly, the warm regions are located north of the main monsoon rainfall maxima (cf. Fig. 3c), while in the regions directly under the monsoon rainfall the ground temperature is relatively cool. This is mainly because of the increased evaporative cooling due to abundant available soil moisture and decreased solar radiation resulting from more cloud cover. Once moist convection sets in, land surface temperature is largely a response to the net surface en-

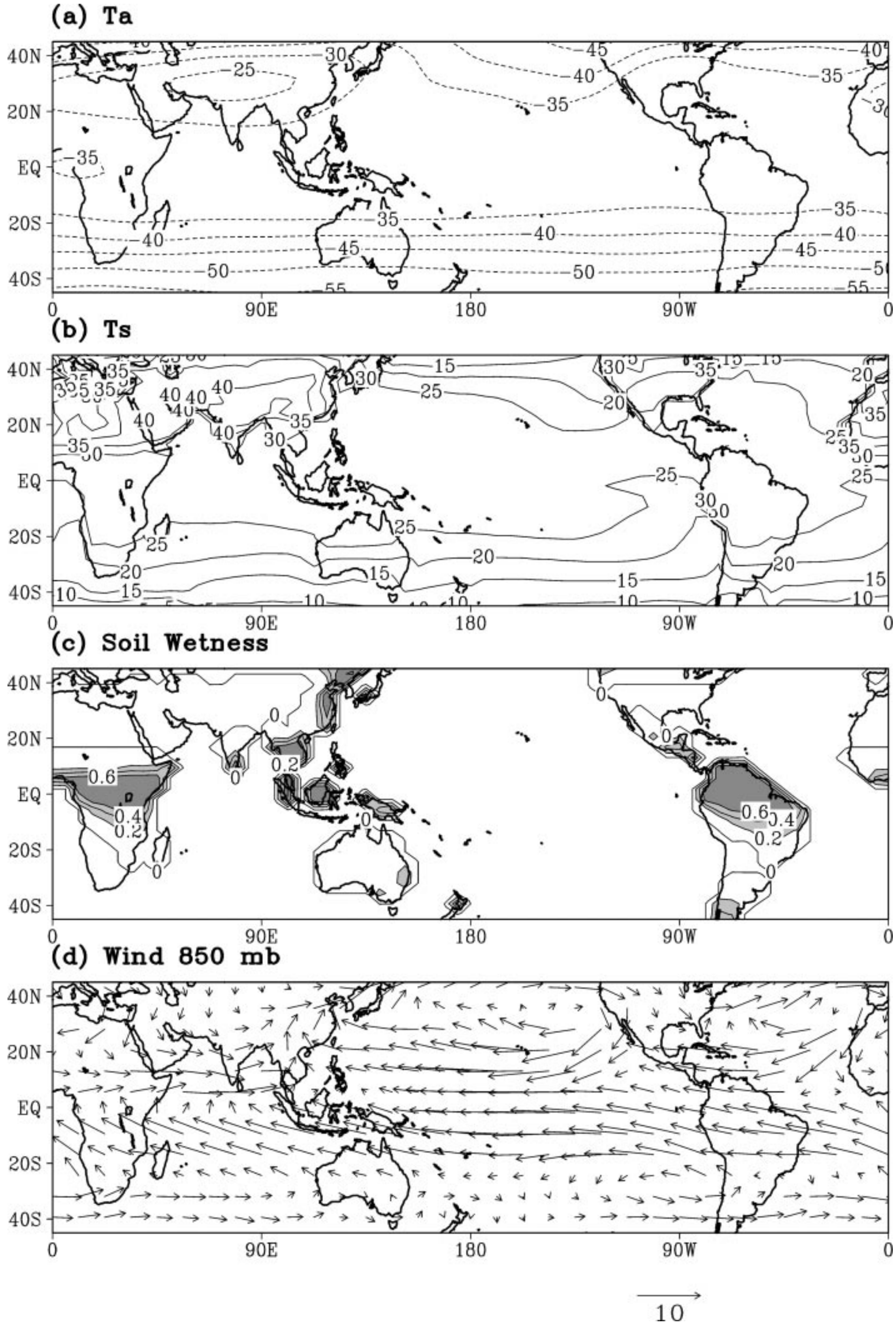

(a) Ta

(b) Ts

(c) Soil Wetness

(d) Wind 850 mb

FIG. 8. Model Jul climatology: (a) air temperature averaged between 500 and 200 mb, contour interval 5°C; (b) surface temperature (simulated ground temperature and observed SST, contour interval 5°C; (c) relative soil wetness *w*, contour interval 0.2, light shading above 0.2 and dark shading above 0.6; (d) 850-mb winds (in m s^{-1}).

ergy and water balance; it does not act as a forcing in the same way SST does (Zeng and Neelin 1999; Webster et al. 1998).

The July soil wetness *w* [Eq. (2.20), soil moisture content normalized by field capacity, Fig. 8c] largely corresponds to the rainfall pattern, showing the wet Tropics and dry subtropics, while midlatitudes also tend to be wet due to the storm rainfall. The memory in soil wetness gives rise to a slow response to rainfall forcing. At typical water flux values, we estimate a memory time of about 1 month to 1 season (see section 3g). The slowness is especially pronounced during the drying periods. An example is seen in the region of Brazil that was under the SACZ during the previous rainy season (Figs. 3a,b), where the signature of northwest–southeast-oriented rainfall pattern still exists in the soil moisture field. Under the intensive tropical convection centers, the maximum soil wetness reaches 0.7. It is not totally saturated because the highly nonlinear subsurface runoff (2.25) is very efficient at removing soil moisture when it is near saturation. An example of the surface water balance for the Amazon basin is given in section 3g.

c. *Sensitivity experiments with model climatology*

As in GCMs, the QTCM has significant dependence on the parameterizations of physical processes. Therefore it is important to establish the sensitivities of the model to its key parameters. On the other hand, the relative simplicity of the model makes it easier to explore the roles of important physical processes through sensitivity and diagnostic studies.

We first show the results from a run with the radiation package clrad1 replaced by the simpler package clrad0 (see section 2b). The major difference is in the cloud prediction and the shortwave scheme (sections 2b, 2e). Figure 9 and Fig. 10 are the counterparts of Fig. 3 and Fig. 5 (cf. observations in Figs. 4 and 6), depicting the simulated precipitation and fluxes of evaporation, OLR, and surface net energy. The rainfall in some of the major convergence centers is slightly stronger in clrad0, such as in the warm pool region, but overall the precipitation patterns are largely similar. Larger differences are seen in the fluxes. The clrad1 version tends to simulate slightly more evaporation than clrad0, while lower OLR minima in the convergence zones are seen in clrad0 (values of less than 220 W m^{-2} are found). The clrad1 version is more realistic in the stratocumulus regions since the stratus clouds are specified (section 2e). Compared to the observations in Fig. 6, both clrad1 and clrad0 somewhat underestimate the net surface flux near the equator with clrad1 slightly less. From now on, the results in this section and the following sections will be taken from the runs using clrad0, and the run shown in Fig. 9 and Fig. 10 will be referred to as the control run.

A model run was conducted with a convective adjustment time τ_c [Eq. (2.17) of NZ] of 8 h rather than 2 h as used in the control run. The January precipitation is shown in Fig. 11. Compared to the control case (Fig. 9a), the tropical convergence zones appear to be slightly weaker, and some local rainfall patterns are somewhat different such as the Amazon–SACZ rainband. However, they are quite similar to each other overall. This modest sensitivity to τ_c is comforting because in real tropical atmosphere, the adjustment time might vary significantly due to mesoscale organization and other disturbances. This insensitivity is rooted in the enthalpy constraint (latent heating comes from water vapor condensation) so that the adjustment time does not enter the moist static energy equation, which tends to determine the large-scale circulation patterns (NZ sections 5b, 7). However, the differences between these runs indicate the extent to which departures from strict QE can affect the simulation at the next level of approximation.

In the QTCM, topographic effects include a contribution to the barotropic vorticity equation as a vorticity source due to the forced topographic lifting when air flows over a mountain [Eqs. (2.7), (4.17), and (4.26), and appendix A of NZ]. This vorticity forcing is zero in the control run with no topography. Figure 12 depicts the July precipitation from a run with this effect included. The most significant differences from the control case (Fig. 9a) are changes in the storm tracks in the North Pacific and North Atlantic. This occurs also in other seasons (not shown), as the topography modifies the stationary waves (e.g., Held 1983), modifying the storm tracks to the east of the continents. The Asian monsoon is somewhat stronger immediately downwind of the Tibetan Plateau in south Asia. There is also some indication of the impact of the Andes on the SACZ and South America rainfall in southern summer. We caution that this implementation of the topographic effects is sensitive to the surface wind evaluation, and validation of stationary wave patterns at midlatitudes has not been carried out.

Details of the evaporation formulation have a large impact on model climatology and variability, as noted in many GCMs (e.g., Palmer et al. 1992). We made a run with the boundary layer wind reduction factor $\eta = 0.2$ in (2.17) so that the modeled evaporation has weaker wind dependence. The run also includes topography, as in Fig. 12. The resulting July precipitation is shown in Fig. 13. The unrealistic, large precipitation maximum around the date line seen in the control run (Fig. 9c) is weaker and has moved westward into the western Pacific warm pool region. The overly strong rainfall over the equatorial Indian Ocean in July [another common deficiency in GCMs as well (Sperber and Palmer 1996)] is somewhat weaker. In contrast, the monsoon over South Asia is noticeably stronger. Further analysis indicates that while this aspect has improved, some other regional aspects have deteriorated in other seasons. Using a lower value of η is no doubt compensating in July for other deficiencies that overestimate the impact of the evaporation–wind feedback on the boundaries of the warm pool. Users desiring an optimal tuning for summer simulations in these regions would be free to explore this sensitivity.

Neelin and Zeng (2000) present the results from a model run with a single land surface type (forest) shown in their Figs. 2–4. Compared to the corresponding fields in the control run (section 3c), the large-scale circulation patterns are in general very similar, but with some re-

(a) January clrad0

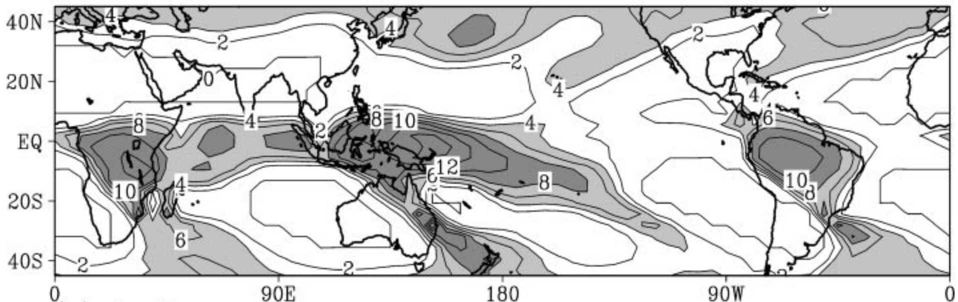

(b) April

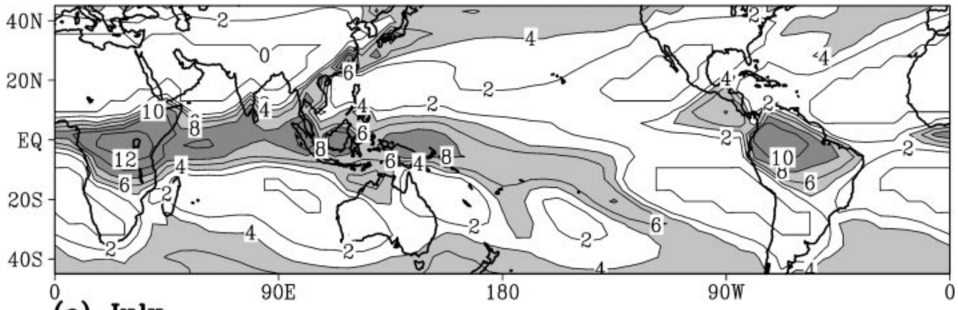

(c) July

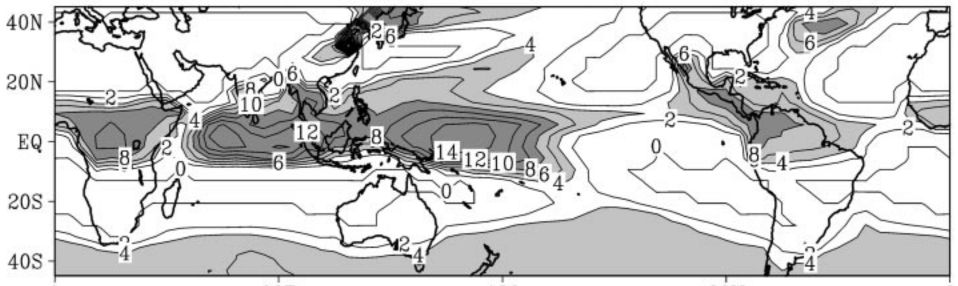

(d) October

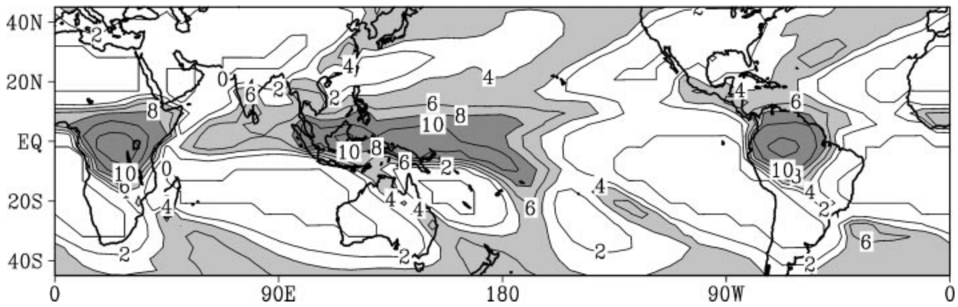

FIG. 9. As in Fig. 3, but for a run using the radiation package clrad0.

gional differences such as the wetter continents. Here we show the results from another run without soil water stress [i.e., $\beta = 1$ or $r_s = r_{s_{\min}}$ in (2.26)]. Depicted in Fig. 14 is the difference in July precipitation between this run and the control run. The most dramatic difference is seen in the enhancement and northward extension of the monsoon over Asia and Africa. This is apparently due to the enhanced convection as a result of extra evaporation over the otherwise relatively dry regions such as the Sahel. The unlimited soil water source is, of course, unrealistic, but this sensitivity experiment nonetheless gives us a general idea of (perhaps) the upper bound of the impact of land surface hydrology. This experiment is somewhat similar to Shukla and Mintz (1982), but the evaporation in the current model is controlled by a minimum stomatal resistance $r_{s_{\min}}$, whereas it was only controlled by a much smaller aerodynamic resistance in their model.

(a) Evap clrad0

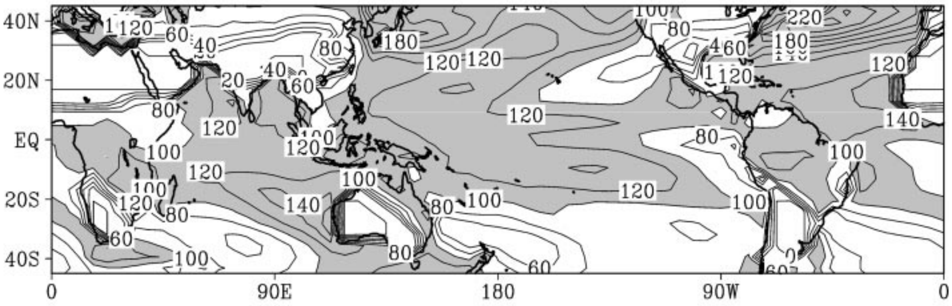

(b) Olr

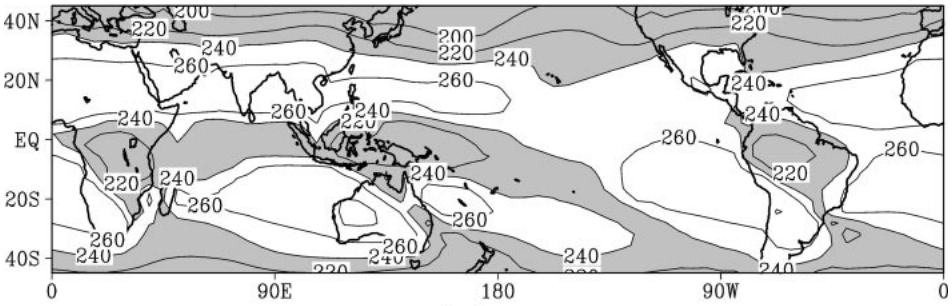

(c) Fs

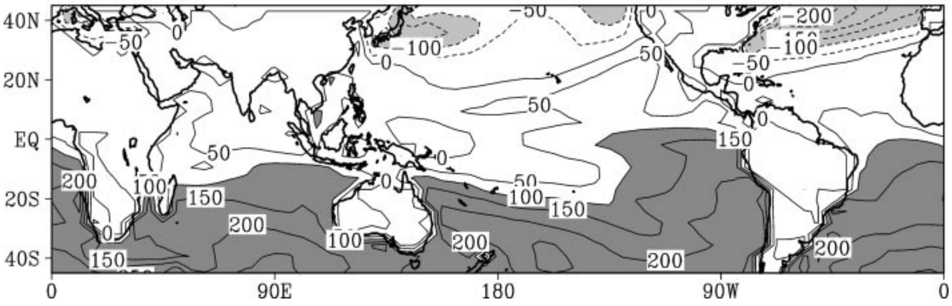

FIG. 10. As in Fig. 5, but for a run using the radiation package clrad0.

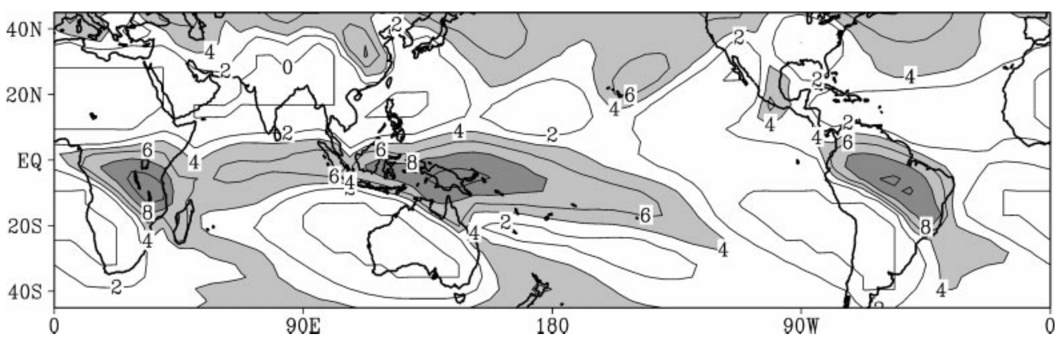

FIG. 11. Jan climatological precipitation as in Fig. 9a, but from a run with the convective adjustment time $\tau_c = 8$ h.

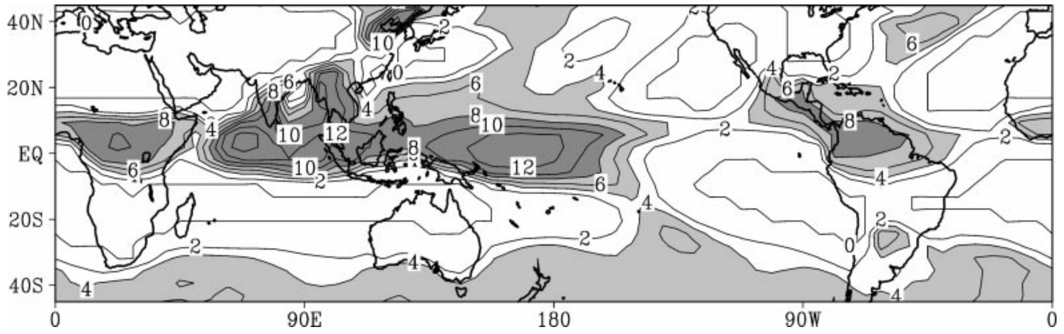

FIG. 12. Jul climatological precipitation as in Fig. 9c, but from a run with topographic stationary wave effects included in the barotropic component.

d. Intraseasonal oscillation

The spectral and spatial characteristics of the intraseasonal variability of an earlier version of the model (β-test version 1.0) are analyzed in Lin et al. (2000), along with excitation mechanisms. Evaporation–wind feedback assists in boosting the variance, but stochastic excitation by midlatitude storms is shown to be a leading factor in maintaining the intraseasonal oscillation in that version. We note that the amplitude of intraseasonal variance is quite sensitive to various parameters, including those affecting midlatitude variance, and the evaporation formulation (2.17). Qualitative aspects of eastward propagation tend to be more robust, although details of the spectrum vary as well as the amplitude. The amplitude of the MJO-like variance is quite weak in the version presented here (version 2.1). In the version of Zeng et al. (2000a) (version 2.0), spectral analysis (not shown) indicates a peak around 50 days at wavenumbers 2 and 3, and eastward propagation is quite apparent. The current version appears to have moist Kelvin-wave-like variability, but the power as a function of wavenumber does not correspond quantitatively to observations (Wheeler and Kiladis 1999).

e. Interannual variability

One of the principal objectives of the QTCM is the simulation of climate variability on interannual timescales. Figure 15 shows the precipitation on the equator from the model during January 1982 to March 1998, while the observations from Xie and Arkin (1996) are shown in Fig. 16. The model captures the major El Niño warm events of 1982/83, 1986/87, 1991/92, and 1997/98, which have anomalies extending all the way across the eastern Pacific, as well as the long-lasting warming events in the first half of the 1990s. The cold La Niña events of 1984, 1988/89, and 1995/96 are also captured. During 1986/87 and 1991/92, the modeled rainfall anomalies in the eastern Pacific are not as strong as in observations, although the eastward extensions in 1982/83 and 1997/98 are reasonable. The maxima around the date line are often too large during the summer. Our sensitivity studies suggest that these are both related to deficiencies in climatology, namely, the weak ITCZ and the maximum around the date line in summer (see discussion in section 3a). An annual modulation of the longer warm or cold events can be seen clearly around the date line, again an indication of the anomaly dependence on the climatology. This annual modulation is also seen in observations, although it is noisier. In addition to rainfall increases directly associated with warm SST during El Niño, the model also captures several aspects of the rainfall reductions in the western Pacific–Indonesian region, and vice versa during La Niña. Over South America and the Atlantic, the correspondence in magnitude and seasonal timing of anom-

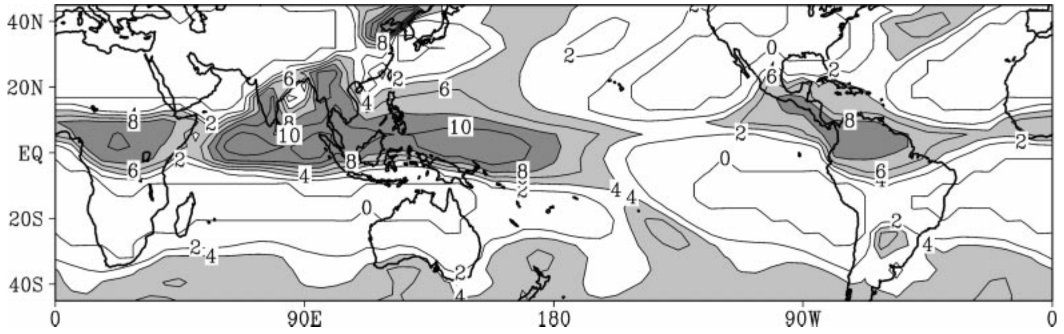

FIG. 13. Jul climatological precipitation as in Fig. 12, but from a run with $\eta = 0.2$ in the evaporation formulation (2.17).

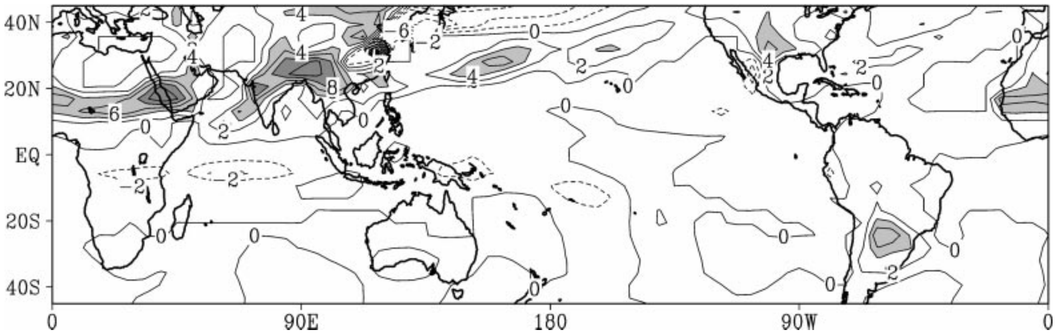

FIG. 14. Difference in Jul climatological precipitation between a run with 100% soil wetness (no water stress) and the control run (Fig. 9c). Contour interval 2 mm day^{-1}, shaded above 4 mm day^{-1}.

alies is imperfect, but the model produces counterparts to several of the major anomalies (e.g., in 1984, 1987, 1988, 1991/92, 1996, and 1997).

In order to see the spatial pattern of the interannual variability, we plot in Fig. 17 a composite winter precipitation difference between three El Niño years (1986/87,1991/92, 1994/95) and three La Niña years (1983/84, 1988/89, 1995/96; warm events minus cold events) for December–January–February and June–July–August. The corresponding observations from Xie and Arkin are shown in Fig. 18. The main positive precipitation anomaly is centered just east of the date line, showing changes in the ITCZ and SPCZ. The model's positive anomaly does not extend quite as far west along the equator as the observations, especially in northern summer, partly related to the larger-than-observed precipitation in the climatology of this region. Surrounding the positive anomaly are negative anomalies over the Indonesian region, extending in a horseshoe pattern to the south and north in the subtropical Pacific. Further away, reduced precipitation is seen over the Amazon and northeastern Australia. In general, the model captures these observed teleconnection patterns, although some details are questionable. Interestingly, some teleconnections to subtropical latitudes are also present, including over southeastern Africa, the enhanced SACZ over Brazil in winter, and the banded structure over and off the coast of east Asia in summer. These presumably involve Rossby wave dynamics, but, at least in the Southern Hemisphere, involve interactions with the convective zones, and so may be more complex than simple external mode Rossby waves (Wallace and Gutzler 1981).

Accompanying the anomalies in convection, the zonal wind stress exhibits large variations associated with ENSO events. Figure 19 shows the time–longitude plot of wind stress anomaly on the equator, while the patterns of an ENSO composite of wind stress anomaly, and model and observed surface zonal wind are shown in Fig. 20. The major wind stress maxima occur around the date line in the Pacific, west of the center of the convection anomalies. Anomalies are also seen over the Atlantic Ocean. Large anomalies of wind stress occur over South America and the Indonesian region because the large surface roughness tends to amplify the effect of wind anomalies. The spatial patterns generally compare well with observations, although the wind stress anomalies off the equator in the subtropical high regions do not have enough meridional component associated with boundary layer turning, and the Kelvin wave induced easterly anomalies to the east of the major ENSO anomaly are a bit too strong. The magnitude of the stress anomalies is also slightly large at times, for instance, during the summer of 1988. The observed midlatitude surface wind anomalies (Fig. 20c) do not show up clearly in the model response. A significant success is the the longitudinal position of the ENSO anomalies, and the variation of the extent and position of these anomalies during the larger El Niños of 1982/83 and 1997/98. Simple models often have difficulty with these aspects, and the dynamics involves the nonlinear simulation of the convecting/nonconvecting boundary. The cloud–radiation package has a significant impact on the stress anomalies: when the clrad1 package is used, very similar spatial patterns of stress are obtained, but with a magnitude of about 0.75 those of Figs. 19 and 20.

Figure 21 shows the correlations between the precipitation, the surface temperature and NINO3 SST calculated using the monthly mean output throughout the 17-yr simulation period. Most features in the precipitation–Niño-3 correlation pattern can be seen in the ENSO composites despite various differences in detail. The correlation is shown since it places more emphasis on regions with smaller but consistent signal, such as some of the teleconnection regions. While the correlation of T_s with Niño-3 over the ocean is simply observation, the model land surface temperature such as over South America shows a strong positive correlation with Niño-3. This is mainly due to decreased evaporative cooling and cloud cover as precipitation over these regions is suppressed, a similar mechanism to that causing ground temperature cooling as the monsoon sets in (section 3f).

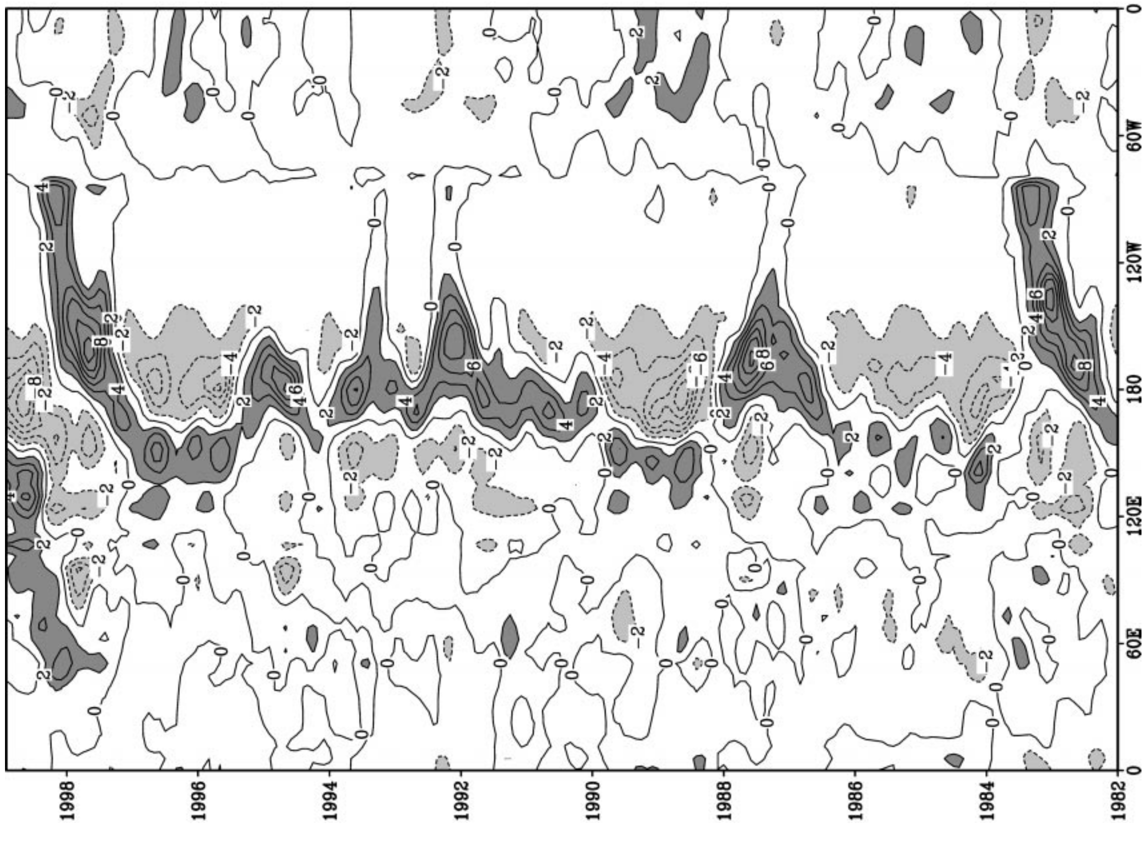

FIG. 15. Model-simulated monthly mean precipitation on the equator through the period 1982–98. Contour interval 2 mm day^{-1}, with dark shading above 2 and light shading below −2.

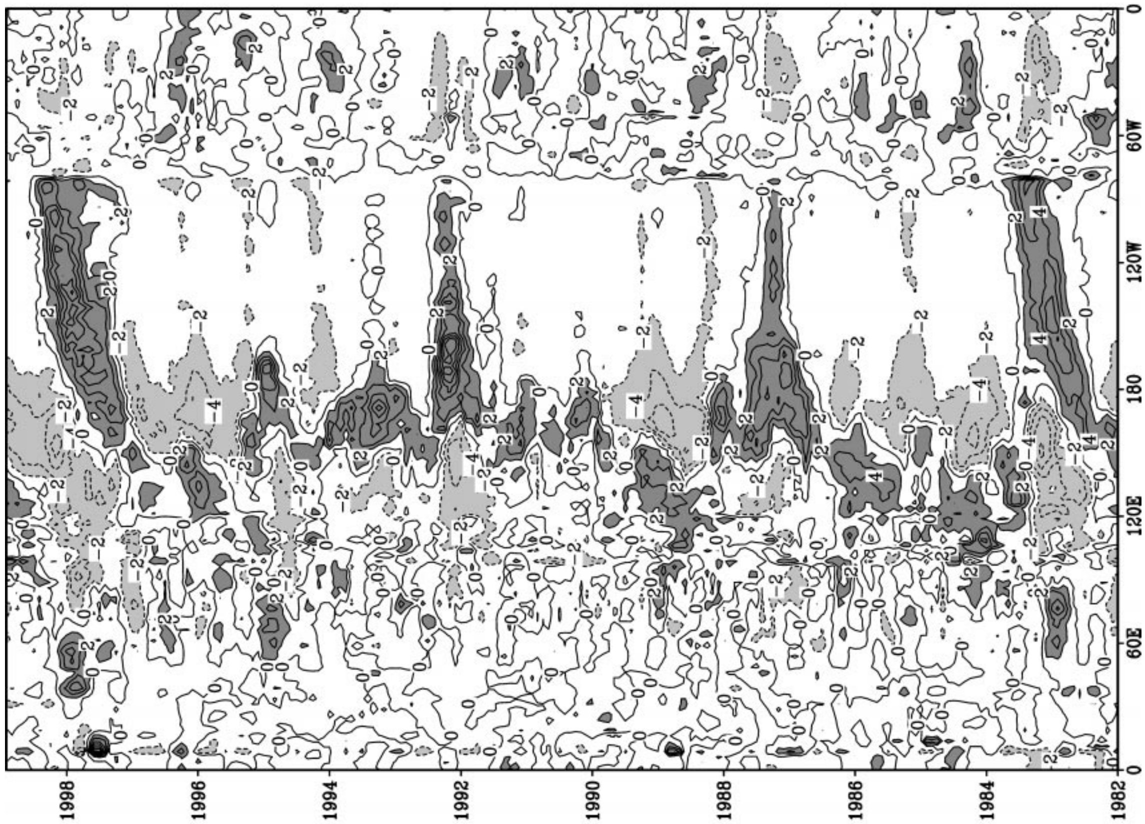

FIG. 16. Same as in Fig. 15, but for the Xie–Arkin observations.

(a) WARM−COLD DJF: QTCM Precip mm/day
(87 92 95) − (84 89 96)

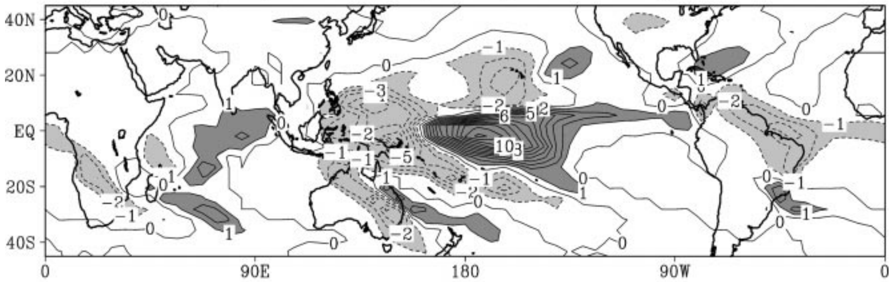

(b) WARM−COLD JJA: QTCM Precip mm/day
(87 92 95) − (84 89 96)

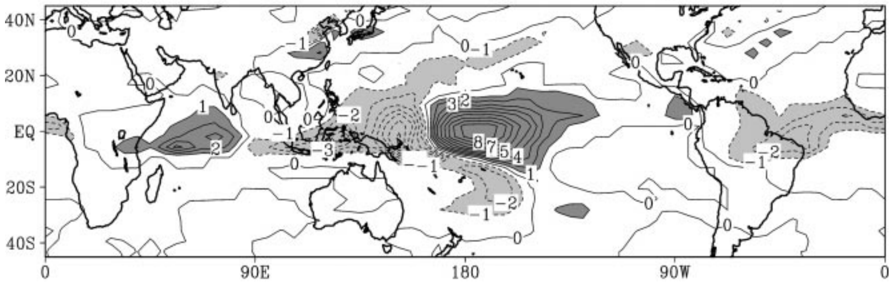

FIG. 17. ENSO composite precipitation differences. Three warm events (1986/87, 1991/92, 1994/95) minus three cold events (1983/84, 1988/89, 1995/96). (a) Northern winter (Dec–Feb), (b) summer (Jun–Aug). Contour interval 1 mm day^{-1}. Dark shading above 1 and light shading below -1 mm day^{-1}.

(a) WARM−COLD DJF: Xie−Arkin Precip mm/day
(87 92 95) − (84 89 96)

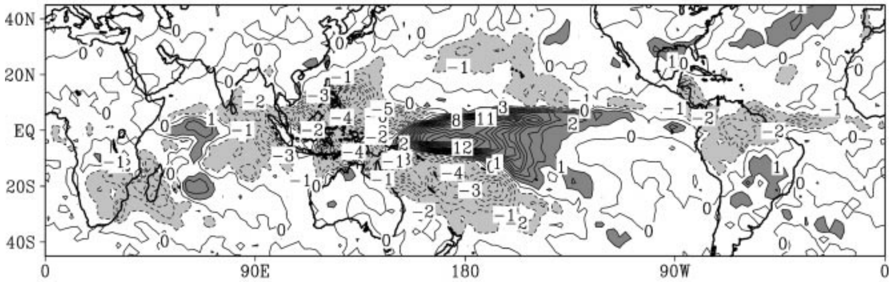

(b) WARM−COLD JJA: Xie−Arkin Precip mm/day
(87 92 95) − (84 89 96)

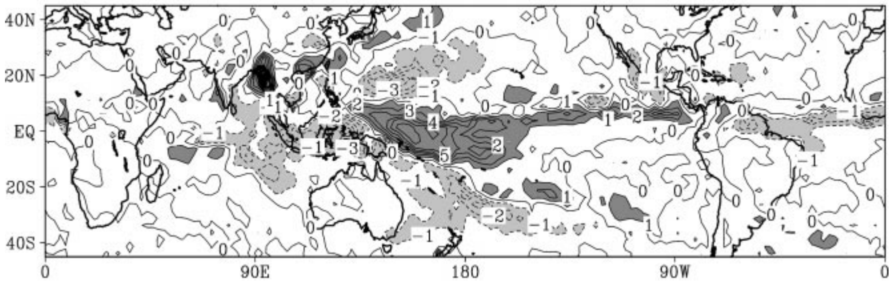

FIG. 18. As in Fig. 17 but from the Xie–Arkin observations.

f. Monsoon: Seasonal cycle and interannual variability

The mature phase of the monsoons has been discussed in section 3a. We now wish to take a closer look at its seasonal evolution and interannual variability. The analysis of the seasonal cycle uses daily output from the climatological SST run, while the interannual variability comes from 10 ensemble runs driven by 1982–98 observed SST.

Figure 22 shows daily values of temperature averaged between 500 and 200 mb, depicting the transition from a baroclinically unstable winter storm regime (seen in signatures of the eastward propagating high frequency storms) to a thermally direct monsoon regime in summer. Warm temperature cores corresponding to the monsoon depressions are well developed both over Asia and North America from July to September, with the one over North America developing slightly later. Close examination indicates that the development of the Asian monsoon trough is a few days delayed compared to the observations of Li and Yanai (1996, Fig. 7a). This is probably related to the weak contrast between land and equatorial ocean (Fig. 9c). The model temperature also exhibits a cold bias everywhere.

Figure 23 shows various fields at 30°N, 112°E; a humid subtropical region in southwestern China; as well as precipitation at 15°N, 100°E. The latter is located within the Southeast Asian monsoon, in an area where the broad features are fairly well simulated but where the time evolution is relatively simple. The point at 30°N represents a region where tropical and midlatitude dynamics are not clearly separated, and it is of interest to see how the model behaves even though the simulation is less accurate. In the climatology (Fig. 9), the rainfall around 30°N is concentrated in a narrow, intense band compared to observed (Fig. 4). The premonsoon season is dry (too dry, since there is no nonconvective or mesoscale rain) before the simulated monsoon onset. The onset occurs in mid-March at 15°N and in mid-June at 30°N. Since the model tends to have less disturbances, the modeled northward progression is smoother compared to observations, in which sudden jumps take place from southern China to the Yangtze River valley and northern China (e.g., Ding 1994). The details of simulated monsoon vary among different model versions (cf. Zeng et al. 2000a), but basic dynamical aspects tend to be similar and illustrate model physics.

The monsoon onset as indicated by the local precipitation occurs after the local solar radiation maximum (shown for 30°N in Fig. 23a) because the monsoon is driven by large-scale heating contrast rather than by the local heating maximum itself, and because moisture must increase sufficiently. At 15°N, the delay is smaller. Monsoon onset corresponds to enough moistening of the atmosphere that q_1 becomes close to T_1 (Fig. 23b). Physically, this corresponds to enough CAPE that the atmosphere has become unstable to moist convection (see sections 4d and 5c of NZ). At 15°N, this aspect is similar (not shown), although simpler, since there is less high-frequency variability, and tropospheric temperature does not rise much before the moisture increase catches up to create CAPE. As the monsoon sets in, evaporation rises from near zero during the premonsoon season, with a spinup time of several days. This is essentially the soil moisture recharge time determined by the precipitation rate and the field capacity [see (2.19)]. The evaporation then lasts much longer after the rain moves away. Along with atmospheric temperature T_1, the ground temperature T_s keeps increasing until monsoon onset and then drops rapidly afterward. This decrease in T_s is well correlated with evaporation, although other factors such as cloud reduction of solar and sensible heat flux also play important roles (e.g., Zeng and Neelin 1999). At 30°N, baroclinic disturbances produce winter rain in addition to the summer monsoon rain.

The monsoons have strong interannual variability and this variability is not in general satisfactorily simulated in GCMs with interannual SST forcing (Sperber and Palmer 1996). It is of great interest to see how the QTCM, a much simpler model but nevertheless with the main physics included, simulates this. In doing so, a practical difficulty is the lack of a universally accepted monsoon index (maybe there is none because of the complexity of the monsoon). Here we choose the Asian monsoon wind shear index (zonal velocity at 850 minus 500 mb in the region 0°–20°N, 40°–110°E) of Webster and Yang (1992). This is a natural index for the present model because it is simply proportional to the strength of the baroclinic component (the barotropic component has constant velocity in the vertical; Fig. 1), which is driven directly by horizontal gradients in the thermodynamics.

An ensemble of 10 model runs that differ only in the initial condition are analyzed. Figure 24 depicts interannual variation of the model simulated Asian monsoon wind shear index averaged for June, July, and August of each year. Unlike most GCMs (Sperber and Palmer 1996), the present model shows variation among the 10 ensemble runs of less than 0.5 m s^{-1}, while the range of interannual variation of this index is about 5 m s^{-1}. This lack of variation among ensemble runs is likely due to omission of some processes responsible for some types of atmospheric internal variability. On the other hand, this lack of ‘‘noise’’ can be an advantage for analysis of the processes and mechanisms the model does represent.

Because the observations contain a significant amount of atmospheric internal variability that is not reproducible, it is not clear to what extent agreement between models forced by SST and observations is expected. The general level of agreement between the QTCM and the observations is similar to what has been found for the GCM simulations in the Atmospheric Model Intercomparison Project (AMIP; Sperber and Palmer 1996). The results show a tendency toward negative correlation

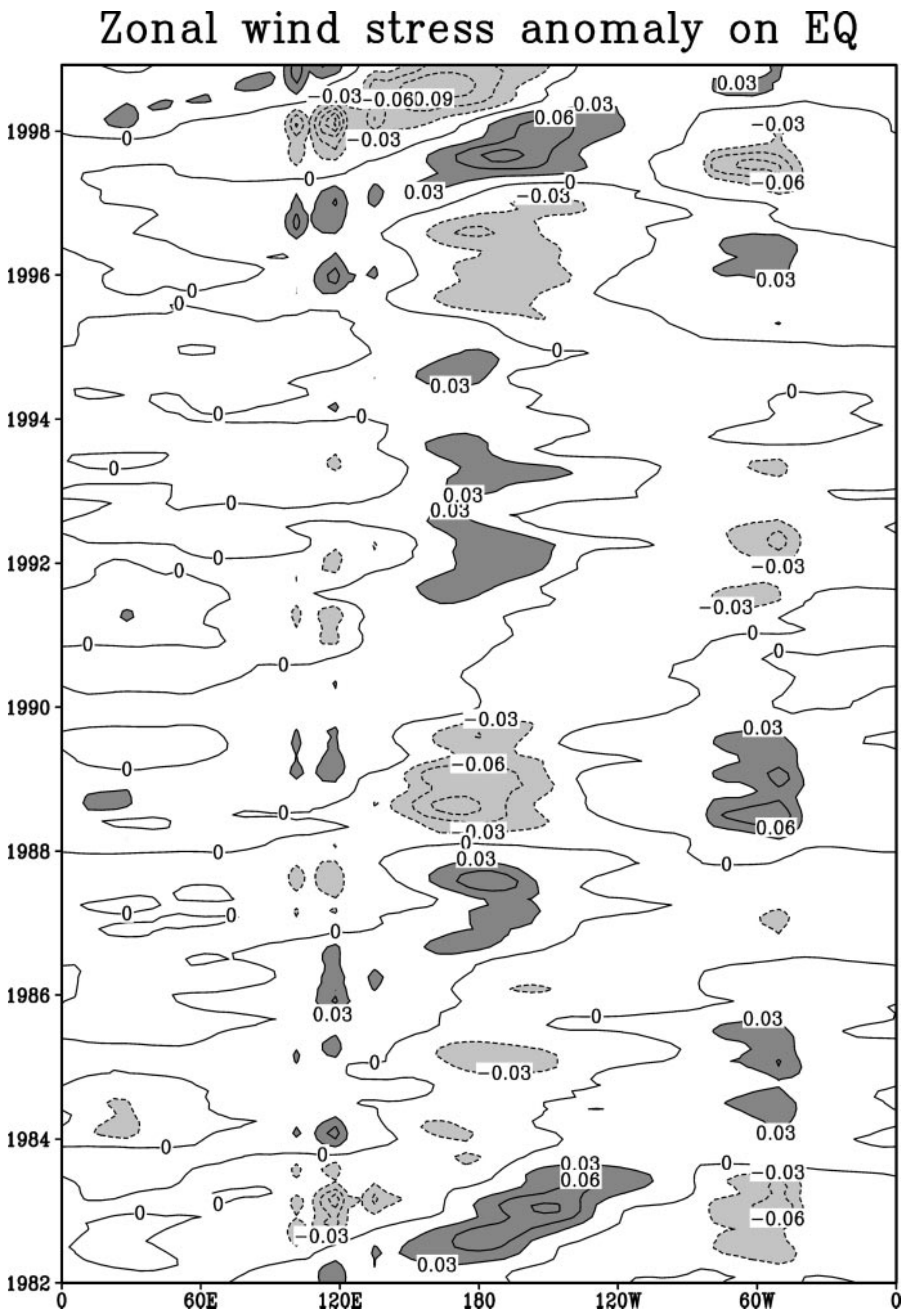

FIG. 19. Model-simulated zonal wind stress on the equator from 1982 to 1998, contour interval 0.03 N m^{-2} with dark shading above 0.03 and light shading below −0.03 N m^{-1}.

with ENSO. For instance, the warm El Niño events in the summers of 1983, 1987, and 1997 correspond to weak monsoon by the wind shear index. The relation with the cold phases is less clear. In 1989 an increase is noted in both model and observations, but this does not hold well in other La Niña years. Since the model does not simulate snow hydrology (section 2d), this level of agreement suggests that the SST may play a more important role in the interannual variability of the large-scale monsoon.

g. Amazon water budget

The strong hydrological cycle in the Amazon basin, with a rainfall rate of over 2000 mm yr^{-1}, provides a test for the land surface model and the convective dy-

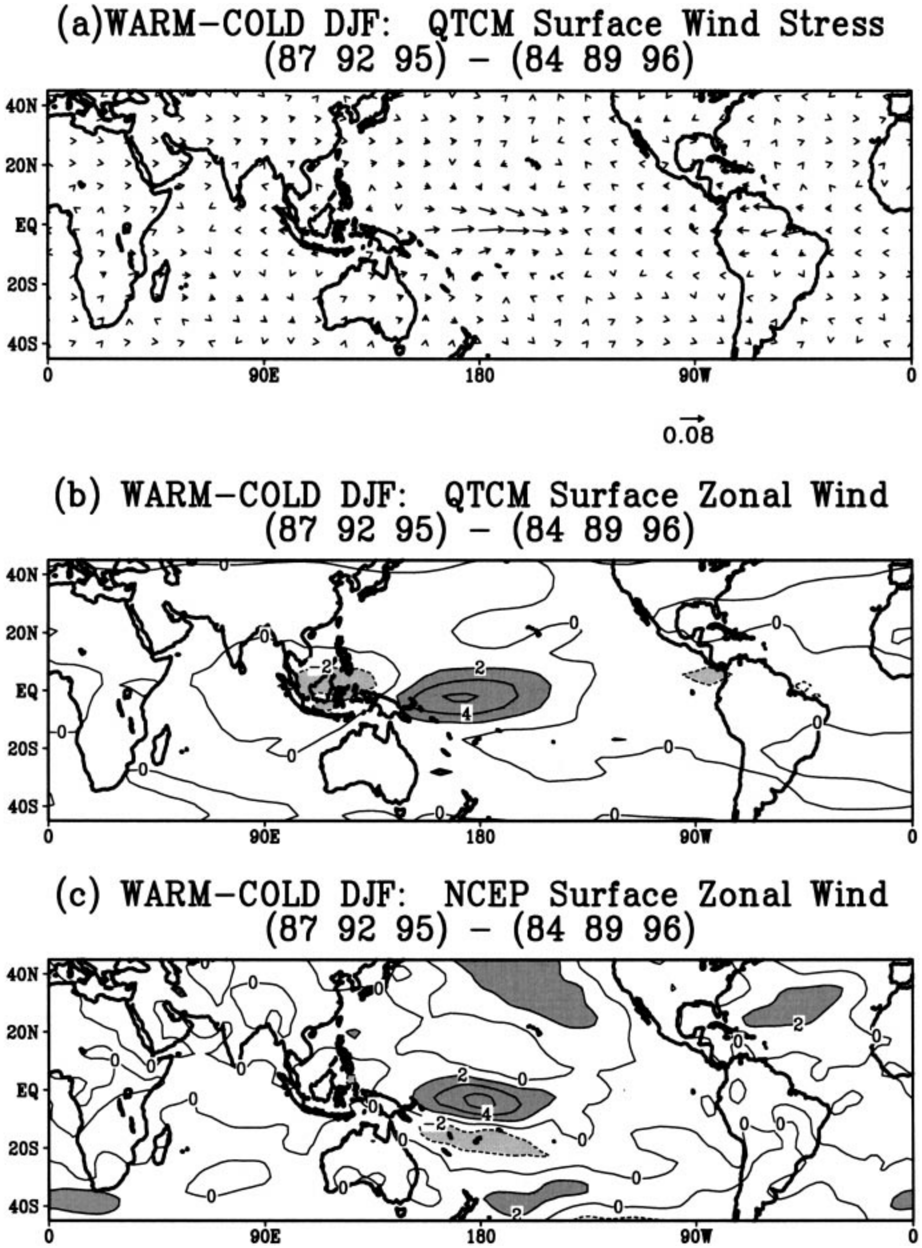

(a)WARM–COLD DJF: QTCM Surface Wind Stress
(87 92 95) – (84 89 96)

(b) WARM–COLD DJF: QTCM Surface Zonal Wind
(87 92 95) – (84 89 96)

(c) WARM–COLD DJF: NCEP Surface Zonal Wind
(87 92 95) – (84 89 96)

FIG. 20. Dec–Feb ENSO composite differences as in Fig. 17a: (a) surface wind stress in N m^{-2}; (b) surface zonal wind in m s^{-1}; (c) as in (b), but from the NCEP–NCAR reanalysis.

namics. Figure 25 shows the model-simulated climatological seasonal hydrological cycle from the 17-yr run. The fields are averaged over the model domain 75°–50°W and 13°S–6°N.

The precipitation shows a strong seasonal cycle, ranging from more than 9 mm day^{-1} during the December–April wet season, to less than 5 mm day^{-1} in the June–September dry season. The rainfall maximum occurs in February, and the minimum in July. These are about 2 mm day^{-1} too large than observations (Zeng 1999, Fig. 5), corresponding to a too wet Amazon all year round as seen in Fig. 9; but the annual variation appears reasonable.

The land surface model is designed to simulate all the major components of the surface hydrological cycle, including the evapotranspiration E_T, interception loss E_I, surface runoff R_s, and subsurface runoff R_g (section 2d). The total evaporation $E = E_T + E_I$ and the total runoff $R = R_s + R_g$ are shown in Fig. 25a, as well as E_I and R_s. The runoff has a similar trend to precipitation, as does interception loss, due to their direct dependence on precipitation. In contrast, the evapotranspiration E_T

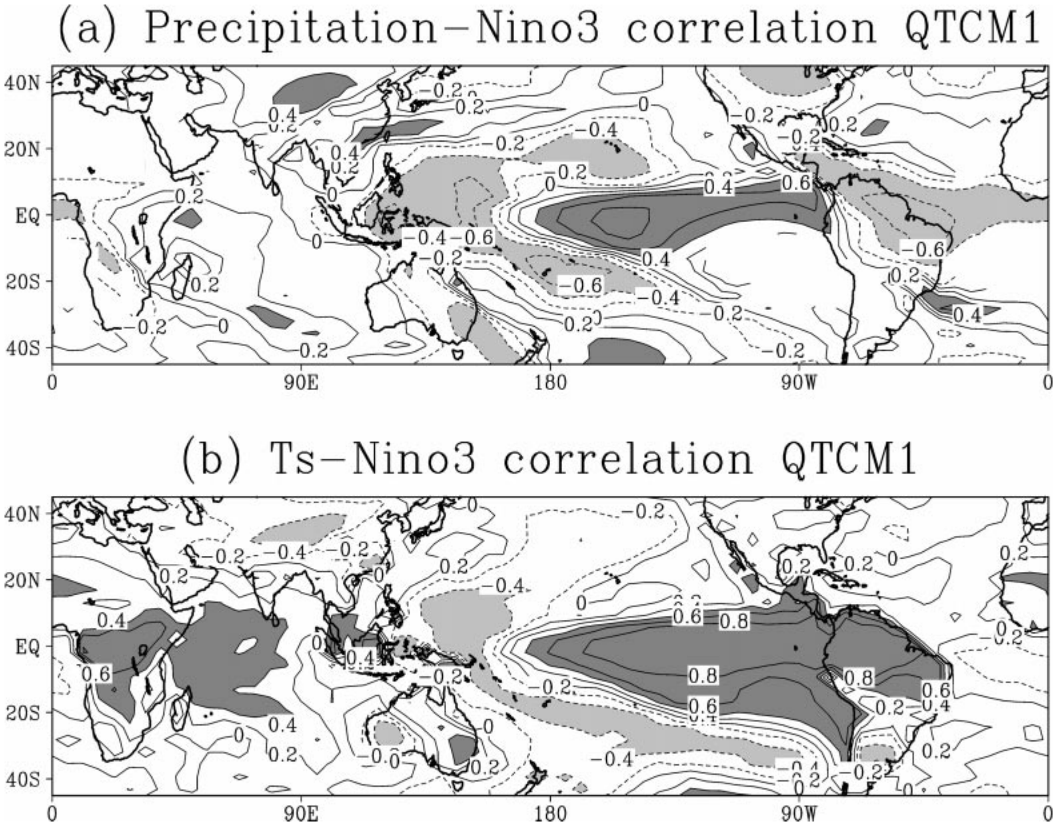

FIG. 21. Correlation between Niño-3 and model-simulated precipitation and surface temperature (observed SST over ocean), calculated using the monthly output for the period 1982–98. Contour interval 0.2, and contours are shaded dark above 0.4 and light below −0.4.

and subsurface runoff R_g depend only on soil moisture, which has a delayed response to surface fluxes due to the memory effect. As can be seen in Fig. 25b, the soil moisture lags behind precipitation by about 2 months, with the driest month occurring in September. The difference between the wettest month (March) and driest month (September) is 100 mm, about a factor of 2 smaller than the diagnosed amplitude based on observed runoff and reanalysis moisture convergence (Zeng 1999). Evaporation decreases slightly toward the end of the dry season in September and is otherwise relatively constant, partly due to the soil moisture memory, partly due to the ¼-power dependence on soil moisture. The latter mimics the deepwater uptake by deep roots. This means the plants are not under significant water stress unless moisture is very low. The simulated near-constant evaporation is in general agreement with measured data in central Amazon (Shuttleworth 1988), although one needs to be cautious about comparing the basin average with the essentially point observation.

As shown in section 3a, the Amazon basin precipitation has a strong correlation with ENSO, as has been identified by many researchers (e.g., Ropelewski and Halpert 1987; Zeng 1999). Figure 26 shows the 12-month running means of various components of the hydrologic cycle. The negative correlation with ENSO is clearly seen in precipitation, runoff, and soil moisture content while evaporation varies only slightly for the reasons discussed above. The interannual variations in P, R, and W can be directly compared to the analyses of Zeng (1999, his Fig. 8). Within the period covered by both, they show similar tendency, but with substantial differences in details, and the overall amplitude is much smaller than observed. For instance, the 1988/89 La Niña event leads to an increase of about 1 mm day^{-1} in precipitation and a corresponding increase in soil water storage.

It is of interest to compare the results here from those of an earlier version of the model (Fig. 13 of Zeng et al. 2000a) where the interannual and seasonal variation in soil moisture and precipitation are much closer to the observations. This is mostly because the atmospheric component of the current model version has a wet bias in the Amazon precipitation, the convective zone not moving as far north in austral winter. The near-saturated soil moisture simply does not change much, an indication of the impact of nonlinearity in land surface hydrology.

A delay on interannual time scales in soil moisture and runoff from precipitation is also noticeable in Fig.

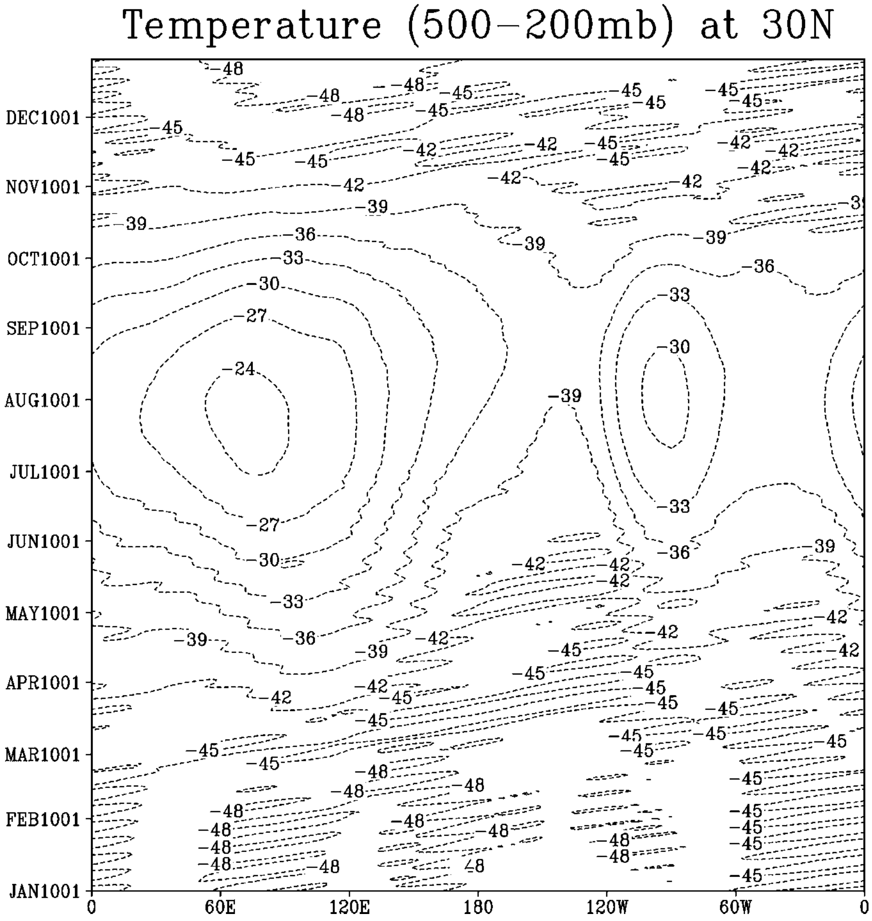

FIG. 22. Evolution of temperature over 1 yr averaged between 200 and 500 mb at 30°N, from the climatological SST run with daily mean output. (In °C.)

26, similar to what was found by Zeng. This memory effect might play a role for season-to-season climate anomalies and act as a link between climate variation in the Pacific and Atlantic (Poveda and Mesa 1997). The atmosphere and land surface models developed here thus provide an efficient tool for studying this type of problem.

4. Conclusions

QTCM1 aims to simulate reasonably complex tropical phenomena with a relatively streamlined tool. A unique feature is that aspects of the dominant subgrid-scale processes, namely, moist convective dynamics, are employed in the model design. Equally important is the balanced treatment of dynamics and other physical processes including cloud and radiation, and land surface processes. In this paper, we present a sample of various results from the first version of the model.

The tropical climatology simulated by QTCM1 appears reasonable, showing the seasonal migration of the tropical convective zones and the variation of the trades. The African and American monsoons are well represented, but the Asian monsoon is somewhat too weak. For a model with only 2 degrees of freedom in the vertical (a baroclinic and a barotropic component), the reconstructed wind fields are quite decent; the good accuracy, despite the high truncation, indicates that the effort spent on the analytical solution prior to turning to numerical methods (see NZ) was well invested. The model does a reasonable job in simulating fields such as surface evaporation, OLR, and net surface energy flux that are representative of the model physical parameterizations. These fields are of importance to coupled ocean–atmosphere modeling and are not usually simulated in simple models.

The simple design of the model makes it relatively easy to conduct extensive sensitivity studies. Tropical convective zones are found sensitive to the evaporation formulation, especially in the western to central Pacific and Indian Oceans. This sensitivity has consequences in the intraseasonal oscillation and the interannual response to ENSO anomalies. The impact of topography on subtropical and midlatitude climate was found significant, especially in the organization of the storm tracks by stationary waves. There are strong influences

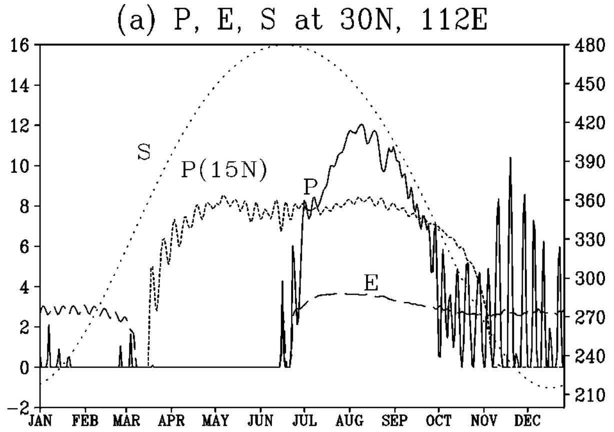

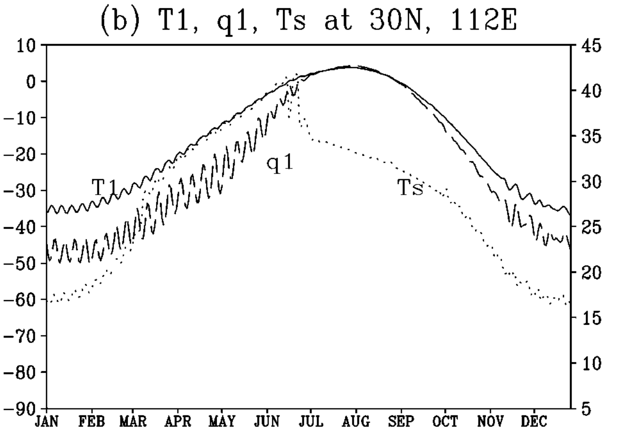

FIG. 23. Various fields at 30°N, 112°E, and precipitation at 15°N, 100°E, representative of the evolution of the Asian monsoon: (a) precipitation P (solid line, mm day^{-1}, labeled on the left axis); evaporation E (dashed line, mm day^{-1}); incoming solar radiation at top *S* (W m^{-2}, dotted line labeled on the right axis); precipitation at 15°N, 100°E (short-dashed line, mm day^{-1}); (b) amplitude of the atmospheric temperature component T_1 (solid line, in Kelvin labeled on the left), amplitude of the humidity component q_1 (dashed line, Kelvin), and the ground temperature T_s (dotted line; °C labeled on the right). See text for discussion.

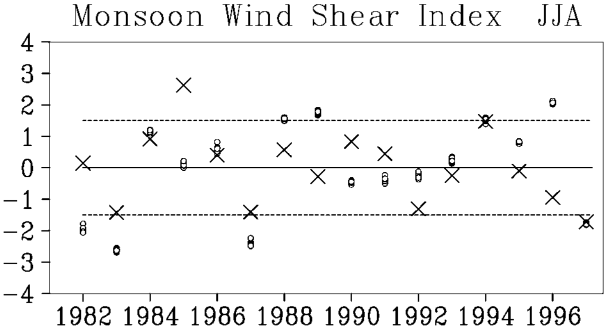

FIG. 24. Interannual variation of the monsoon wind shear index (difference between the winds at 850 and 250 mb over the region 0°–20°N, 70°–120°E) as defined by Webster and Yang (1992) for the months Jun–Aug. Open circles are results from an ensemble of 10 model runs differing only by their initial conditions, while crosses are results from the NCEP–NCAR reanalysis.

on regional climate from various aspects of land surface processes, such as fewer land surface types and different representations of surface hydrology, but the global pattern proves quite robust to these effects.

A multiyear model run driven by the observed SST anomaly from 1982 to 1998 demonstrates the model's ability to simulate the atmospheric interannual response in precipitation and other key fields. The primary ENSO rainfall anomalies are simulated near the dateline, extending farther eastward during large warm events. Also simulated are the reduced rainfall regions in the tropical western Pacific–Indonesian region, and South America. Certain subtropical teleconnections are also captured. Differing teleconnection mechanisms over land and ocean regions in response to ENSO anomalies are noted. These involve feedbacks from moist convection, cloud–radiative effects, and land surface processes, as will be described elsewhere.

The evolution of the Asian monsoon depicts the transition from the winter baroclinically unstable regime to the summer thermally direct circulation regime. The monsoon onset occurs successively northward, with a hint of intraseasonal variations. Regional features and monsoon evolution are found sensitive to model physics, with significant differences among model versions. Noting this caveat, a number of physical processes including evaporation, convection, land surface energy,

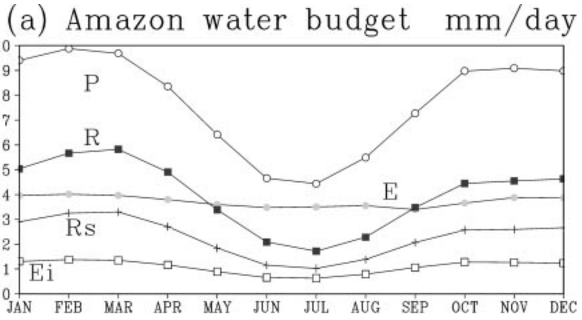

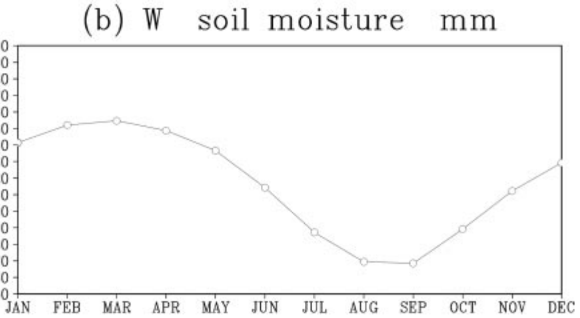

FIG. 25. Seasonal hydrologic cycle averaged over the Amazon basin: (a) precipitation *P* (open circles), total evaporation *E* (filled circles), interception loss E_i (open squares), total runoff *R* (filled squares), surface runoff R_s (crosses) (all in mm day^{-1}); (b) soil moisture content *W* (in mm).

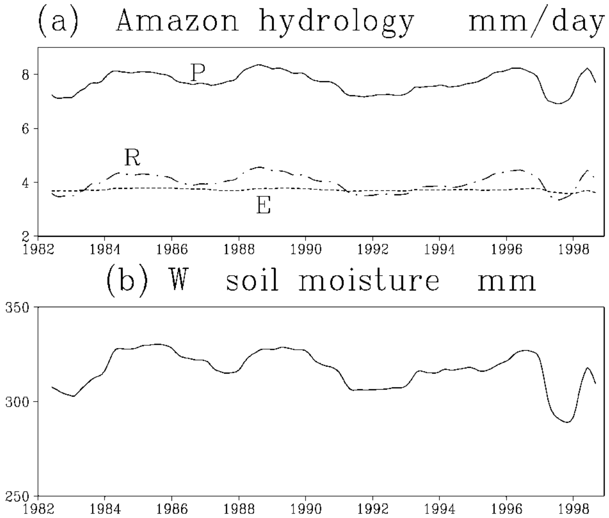

FIG. 26. Interannual variations of the hydrologic cycle over the Amazon basin: (a) precipitation P (solid line), evaporation E (dashed line), runoff R (dash-dotted line) (all in mm day^{-1}); (b) soil moisture content W (in mm). The monthly data are low-pass filtered by a 12-month running mean.

and hydrologic processes show interesting responses and feedbacks. For instance, a drop in land temperature occurs in response to evaporation and cloud–radiative effects after monsoon onset. If soil moisture is artificially set to saturation, the monsoon onset occurs earlier and the monsoon is stronger, indicating the potential importance of surface hydrology. The model monsoon wind shear index as defined by Webster and Yang (1992) shows significant interannual variability and some correlation with ENSO warm events. The behavior and level of agreement with observations are similar to those of GCMs in the AMIP. This suggests a significant role of SST variations in influencing the land–sea thermal contrast, with feedbacks from land processes.

Aspects of the land surface model SLand are analyzed using the water budget over the Amazon basin. The land surface hydrology is influenced by both the land surface parameterization and the atmospheric component of the hydrologic cycle, especially the simulated precipitation. The components of the seasonal water cycle including precipitation, evapotranspiration, interception loss, and surface and subsurface runoff appear reasonable compared to recent observational analyses. On interannual timescales, the Amazon hydrologic cycle exhibits a correlation with ENSO. The amplitude of interannual soil moisture variation is sensitive to model climatology due to nonlinear effects in soil moisture physics.

Having originally derived the model framework with theoretical applications in mind, the quantitative simulation presented here seems better than originally anticipated. The climatology of tropical precipitation, while imperfect with respect to observations, appears to be better than that of several GCMs of the previous generation, of comparable resolution. This includes the Geophysical Fluid Dynamics Laboratory R15 model as analyzed in Lau (1985), the older UCLA GCM version (Mechoso et al. 1987), and community climate model (CCM) versions CCM1 and CCM2 (Hurrell et al. 1993). Since these GCMs have proven their worth in many studies, the comparison is encouraging. For certain fields or phenomena, the simulation is comparable enough to current GCMs to be useful. Obviously, the QTCM solves a less complex problem than the GCMs; the point is simply that QTCM1 can reproduce certain results studied in GCMs but within a system that is more accessible to theoretical analysis.

In developing the model, including the cloud–radiative parameterizations and land surface model, we were always aware of the parallel with earlier GCM work. Have we merely revamped a two-layer GCM in Galerkin form? Some important differences include an underlying analytical solution of the primitive equations plus deep convective parameterization that holds under certain conditions; a connection to parcel buoyancy considerations in the convective parameterization by reduction of CAPE, even in the projected system; more general vertical structures, including cloud types, than are normally admitted in level or layer models; and formulation and parameterizations that are designed to be reducible into even simpler versions for analysis. The model also contains an underlying physical hypothesis about the dominant effects in the tropical general circulation, outlined in more detail in N97 and NZ. The effect of deep convection in communicating surface warming through the troposphere is seen via the effect upon pressure gradients of pulling temperature toward a moist convective profile. Column energy and moisture budgets, together forming the moist static energy budget, are important in setting the degree to which dynamics can flatten out these pressure gradients. The reasonable success of the model in quantitative simulation of many of the major tropical climate phenomena is suggestive that this view of the tropical circulation can be productive.

The simulation of aspects of tropical climate and variability indicates the usefulness of filling the modeling niche between simple models and GCMs. As discussed in N97 and NZ, certain simplifications of QTCM1 offer justification for why some simple models had reasonable success in the past. Now, because the execution time is fast, and the analysis almost as easy as in simple models, especially in convective zones, we can offer QTCM1 to the community to replace simple models in applications where consistent energetics and convective physics are important, or where better description of cloud, radiation, and land processes is desired.

Acknowledgments. This work was supported in part by National Science Foundation Grant ATM-9521389 and National Oceanic and Atmospheric Administration Grant NA46GP0244. Early stages of this work were carried out while the authors were visiting the Massachusetts Institute of Technology, Department of Earth

Atmospheric and Planetary Sciences; JDN acknowledges support from the Houghton Lectureship. Conversations with A. Arakawa, C. Bretherton, R. Dickinson, P. Dirmeyer, K. Emanuel, R. Koster, K.-N. Liou, C. R. Mechoso, D. A. Randall, A. Sobel, R. Seager, J. Shuttleworth, P. Webster, M. Yanai, and S. Zebiak were helpful. Thanks are due to other group members who have been involved in this project or contributed comments: A. Adcroft, J. Lin, M. Munnich, W. Weibel, J.-Y. Yu, and especially H. Su. We thank those in other groups involved in ''beta-testing'' of the code for their patience and feedback, notably C. Cassou, H.-R. Chang, and C. Perigaud.

REFERENCES

Betts, A. K., and M. J. Miller, 1986: A new convective adjustment scheme. Part II: Single column tests using GATE wave, BOMEX, ATEX and arctic air-mass data sets. *Quart. J. Roy. Meteor. Soc.,* **112,** 693–709.

——, and ——, 1993: The Betts–Miller scheme. *The Representation of Cumulus Convection in Numerical Models, Meteor. Monogr.,* No. 46, Amer. Meteor. Soc., 107–121.

Bras, R. L., 1990: *Hydrology: An Introduction to Hydrologic Science.* Addison-Wesley, 643 pp.

Budyko, M. I., 1974: *Climate and Life.* Academic Press, 508 pp.

Chou, C., 1997: Simplified radiation and convection treatments for large-scale tropical atmospheric modeling. Ph.D. dissertation, University of California, Los Angeles, Los Angeles, CA, 215 pp. [Available from University of California, Los Angeles, Los Angeles, CA 90095-1565.]

——, and J. D. Neelin, 1996: Linearization of a longwave radiation scheme for intermediate tropical atmospheric models. *J. Geophys. Res.,* **101,** 15 129–15 145.

Darnell, W. L., W. F. Staylor, S. K. Gupta, N. A. Ritchey, and A. C. Wilber, 1992: Seasonal variation of surface radiation budget derived from international satellite cloud climatology project C1 data. *J. Geophys. Res.,* **97,** 15 741–15 760.

Deardorff, J. W., 1972: Parameterization of the planetary boundary layer for use in general circulation models. *Mon. Wea. Rev.,* **100,** 93–106.

Delworth, T. L., and S. Manabe, 1993. Climate variability and land-surface processes. *Adv. Water Resour.,* **16,** 3–20.

Dickinson, R. E., A. Henderson-Sellers, and P. J. Kennedy, 1993: Biosphere–Atmosphere Transfer Scheme (BATS) Version 1e as coupled to the NCAR Community Climate Model. NCAR Tech. Note NCAR/TN-387+STR, NCAR, Boulder, CO, 72 pp.

Ding, Y.-H., 1994: *Monsoons over China.* Kluwer Academic, 419 pp.

Entekhabi, D., and P. S. Eagleson, 1989: Land surface hydrology parameterization for atmospheric general circulation models including subgrid scale spatial variability. *J. Climate,* **2,** 816–831.

Esbensen, S. K., and M. J. McPhaden, 1996: Enhancement of tropical ocean evaporation and sensible heat flux by atmospheric mesoscale systems. *J. Climate,* **9,** 2307–2325.

Fu, Q., and K. N. Liou, 1993: Parameterization of the radiative properties of cirrus clouds. *J. Atmos. Sci.,* **50,** 2008–2025.

Garratt, J. R., 1992: *The Atmospheric Boundary Layer.* Cambridge University Press, 316 pp.

Gill, A. E., 1980: Some simple solutions for heat induced tropical circulation. *Quart. J. Roy. Meteor. Soc.,* **106,** 447–462.

Harshvardhan, R. Davies, D. A. Randall, and T. G. Corsetti, 1987: A fast radiation parameterization for general circulation models. *J. Geophys. Res.,* **92,** 1009–1016.

Held, I. M., 1983: Stationary and quasi-stationary eddies in the extratropical troposphere: Theory. *Large Scale Dynamical Processes in the Atmosphere,* B. J. Hoskins and R. Pearce, Eds., Academic Press, 127–168.

Hurrell, J. W., J. J. Hack, and D. P. Baumhefner, 1993: Comparison of NCAR Community Climate Model (CCM) climates. NCAR Tech. Note TN-395+STR, NCAR, Boulder, CO, 335 pp.

Kalnay, E., and Coauthors, 1996: The NCEP/NCAR 40-Year Reanalysis Project. *Bull. Amer. Meteor. Soc.,* **77,** 437–471.

Kiehl, J. T., 1992: Atmospheric general circulation modeling. *Climate System Modeling,* K. E. Trenberth, Ed., Cambridge University Press, 319–370.

Koster, R. D., and P. C. D. Milly, 1997: The interplay between transpiration and runoff formulations in land surface schemes used with atmospheric models. *J. Climate,* **10,** 1578–1591.

Lau, N.-C., 1985: Modeling the seasonal dependence of the atmospheric response to observed El Niños in 1962–76. *Mon. Wea. Rev.,* **113,** 1970–1996.

Lean, J., C. B. Bunton, C. A. Nobre, and P. R. Rowntree, 1996: The simulated impact of Amazonian deforestation on climate using measured ABRACOS vegetation characteristics. *Amazonian Deforestation and Climate,* J. H. C. Gash et al., Eds., John Wiley, 549–576.

Li, C., and M. Yanai, 1996: The onset and interannual variability of the Asian summer monsoon in relation to land–sea thermal contrast. *J. Climate,* **9,** 358–375.

Lin, J. W.-B., J. D. Neelin, and N. Zeng, 2000: Maintenance of tropical intraseasonal variability: Impact of evaporation–wind feedback and midlatitude storms. *J. Atmos. Sci.,* in press.

Liou, K.-N., 1980: *An Introduction to Atmospheric Radiation.* Academic Press, 392 pp.

Manabe, S., J. Smagorinsky, and R. F. Strickler, 1965: Simulated climatology of a general circulation model with a hydrological cycle. *Mon. Wea. Rev.,* **93,** 769–798.

Mechoso, C. R., A. Kitoh, S. Moorthi, and A. Arakawa, 1987: Numerical simulations of the atmospheric response to a sea surface temperature anomaly over the equatorial eastern Pacific Ocean. *Mon. Wea. Rev.,* **115,** 2936–2956.

Neelin, J. D., 1997: Implications of convective quasi-equilibrium for the large-scale flow. *The Physics and Parameterization of Moist Atmospheric Convection,* R. K. Smith, Ed., Kluwer Academic, 413–446.

——, and N. Zeng, 2000: A quasi-equilibrium tropical circulation model—Formulation. *J. Atmos. Sci.,* **57,** 1741–1766.

Oberhuber, J. M., 1988: An atlas based on the COADS data set: The budgets of heat buoyancy and turbulent kinetic energy at the surface of the global ocean. Max-Planck-Institut für Meteorologie Rep. 15. [Available from Max-Plank-Institut für Meteorologie, Bundesstrasse 55, D-2000, Hamburg 13, Germany.]

Palmer, T. N., C. Brankovic, P. Viterbo, and M. J. Miller, 1992: Modeling interannual variations of summer monsoons. *J. Climate,* **5,** 399–417.

Poveda, G., and O. J. Mesa, 1997: Feedbacks between hydrological processes in tropical South America and large-scale ocean–atmosphere phenomena. *J. Climate,* **10,** 2690–2702.

Reynolds, R. W., and T. M. Smith, 1994: Improved globalsea surface temperature analyses using optimum interpolation. *J. Climate,* **7,** 929–948.

Ropelewski, C. F., and M. S. Halpert, 1987: Global and regional scale precipitation associated with El Niño/Southern Oscillation. *Mon. Wea. Rev.,* **115,** 1606–1626.

Rossow, W. B., and R. A. Schiffer, 1991: ISCCP cloud data products. *Bull. Amer. Meteor. Soc.,* **72,** 2–20.

Sato, N., P. J. Sellers, D. A. Randall, E. K. Schneider, J. Shukla, J. L. Kinter III, Y.-T. Hou, and E. Albertazzi, 1989: Effects of implementing the Simple Biosphere Model in a general circulation model. *J. Atmos. Sci.,* **46,** 2757–2782.

Sellers, P. J., and Coauthors, 1996: A revised land surface parameterization (SiB2) for atmospheric GCMs. Part I: Model formulation. *J. Climate,* **9,** 676–705.

Shao, Y., and A. Henderson-Sellers, 1996: Modeling soil moisture: A project for intercomparison of land surface parameterization schemes phase 2(b). *J. Geophys. Res.,* **101,** 7227–7250.

Shukla, J., and Y. Mintz, 1982: Influence of land-surface evapotranspiration on the earth's climate. *Science,* **215,** 1498–1501.

Shuttleworth, W. J., 1988: Evaporation from Amazonian rain forest. *Proc. Roy. Soc. London,* **233B,** 321–346.

Sperber, K. R., and T. N. Palmer, 1996: Interannual tropical rainfall variability in general circulation model simulations associated with the Atmospheric Model Intercomparison Project. *J. Climate,* **9,** 2727–2750.

Wallace, J. M., and D. S. Gutzler, 1981: Teleconnections in the potential height field during the Northern Hemisphere winter. *Mon. Wea. Rev.,* **109,** 784–812.

Wang, B., and T. Li, 1993: A simple tropical atmospheric model of relevance to short-term climate variation. *J. Atmos. Sci.,* **50,** 260–284.

Webster, P. J., and S. Yang, 1992: Monsoon and ENSO: Selectively interactive systems. *Quart. J. Roy. Meteor. Soc.,* **118,** 877–926.

——, V. Magaña, T. N. Palmer, J. Shukla, R. Tomas, M. Yanai, and T. Yasunari, 1998: Monsoons: Processes, predictability, and the prospects for prediction. *J. Geophys. Res.,* **103,** 14 451–14 510.

Wheeler, M., and G. N. Kiladis, 1999: Convectively coupled equatorial waves: Analysis of clouds and temperature in the wavenumber–frequency domain. *J. Atmos. Sci.,* **56,** 374–399.

Xie, P., and P. A. Arkin, 1996: Analyses of global monthly precipitation using gauge observations, satellite estimates, and numerical model predictions. *J. Climate,* **9,** 840–858.

Zeng, N., 1999: Seasonal cycle and interannual variability in the Amazon hydrologic cycle. *J. Geophys. Res.,* **104** (D8), 9097–9106.

——, and J. D. Neelin, 1999: A land–atmosphere interaction theory for the tropical deforestation problem. *J. Climate,* **12,** 857–872.

——, ——, C. Chou, J. W.-B. Lin, and H. Su, 2000a: Climate and variability in a quasi-equilibrium tropical circulation model. *General Circulation Modeling: Past, Present, and Future,* D. A. Randall, Ed., Academic Press, 416 pp.

——, J. W. Shuttleworth, and J. H. C. Gash, 2000b: Influence of temporal variability of rainfall on interception loss: I. Point analysis. *J. Hydrol.,* in press.